COMPUTATIONAL PULSATILE FLOW AND EFFICIENCY ANALYSIS OF BIOCOMPATIBLE MICROFLUIDIC ARTIFICIAL LUNGS FOR DIFFERENT FIBER CONFIGURATIONS

by
Ahmet Yusuf Asiltürk
B.S., Mechanical Engineering, Boğaziçi University, 2019

Submitted to the Institute for Graduate Studies in
Science and Engineering in partial fulfillment of
the requirements for the degree of
Master of Science

Graduate Program in Computational Science and Engineering
Boğaziçi University
2023

ACKNOWLEDGEMENTS

First and foremost, I must acknowledge my limitless thanks to Allah for his help, guidance, and bless by giving me the opportunity to complete this thesis.

I am extremely grateful to my supervisor Prof. Kunt Atalık for his invaluable advice and continuous support during my study. His immense knowledge and plentiful experience have encouraged me in all the time of my academic research. I will always appreciate his efforts and consider myself fortunate to have such a concerning mentor.

I would like to thank Taha Küçükkatırcı, Enes Yalçın, Hüseyin Arslan, Melih Demirci, Semih Öncel, and Asım Gümüş for all the times we had throughout my studies. Special thanks to them for always being there for me to help no matter how busy they are.

I would like to thank and commemorate my grandfather, Oğuzhan Asiltürk, who passed away during my master's studies. The way he motivated me was invaluable.

Last but definitely not the least, my deepest and most sincere gratitude goes to my family. Words cannot fully express the extent of my appreciation for their unwavering support and encouragement throughout my academic journey. My mother, Nagehan Gül Asiltürk, instilled in me a passion for science and a desire to make a positive impact on the world from a young age. My father, Murad Asiltürk, taught me the importance of both morality and analytical thinking, which have been invaluable assets in my studies. My sisters, Zeynep and Meryem, and my brother Oğuzhan, have always been a constant source of support and encouragement, and I am forever grateful for their love and guidance. I would not have achieved this success without them.

Finally, financial support provided by TÜBİTAK BİDEB 2210-A is acknowledged.

ABSTRACT

COMPUTATIONAL PULSATILE FLOW AND EFFICIENCY ANALYSIS OF BIOCOMPATIBLE MICROFLUIDIC ARTIFICIAL LUNGS FOR DIFFERENT FIBER CONFIGURATIONS

Average-sized microfluidic artificial lungs consisting of rows and columns of fiber bundles with the different column to row aspect ratios (AR) are numerically analyzed for flow characteristics, maximum gas transfer performance, minimum pressure drop, and proper wall shear stress (WSS) values in terms of biocompatibility. The flow is fully laminar and assumed to be incompressible. The problem is solved with both Newtonian and Non-Newtonian Carreau models. The transport analysis is performed using a combined convection-diffusion model, and the numerical simulations are carried out with the finite element method. The inlet volumetric flow is modeled as a sinusoidal wave function to simulate the cardiac cycle and its effect on the device performance. The model is first validated with experimental studies in steady-state condition and compared with existing correlations for transient conditions. Then, the validated model is used for a parametric study in both steady and pulsatile flow conditions. The results show that increasing the aspect ratio in fiber configuration leads to converging gas transfer rate, higher pressure drop, and higher WSS. While determining the optimum configuration, the acceptable shear stress levels play a decisive role to ensure biocompatibility. Also, it is observed that the steady analysis underestimates the gas transfer for higher aspect ratios. The Newtonian model finds the pressure drop and shear stress values less than the Carreau model. In contrast, the oxygen transfer performance observed in the Newtonian model is overestimated approximately by 5% compared to the Carreau model predictions.

ÖZET

FARKLI FİBER KONFİGÜRASYONLARI İÇİN BİYOUYUMLU MİKROAKIŞKAN YAPAY AKCİĞERLERİN HESAPLAMALI PULSATİL AKIŞ VE VERİMLİLİK ANALİZİ

Ortalama boyutta bir mikro akışkan yapay akciğerin farklı sütn-sıra en-boy oranlarındaki konfigürasyonları; akış özellikleri, gaz transfer performansı, basınç kaybı, ve biyouyumluluğu sağlayan uygun duvar kayma gerilimlerinin incelenmesi için nümerik olarak analiz edilmektedir. Akış tamamen laminerdir ve sıkıştırılamaz olduğu varsayılmaktadır. Problemin çözümü hem Newtonyen hem de Newtonyen olmayan Carreau model ile yapılmaktadır. Gaz transferi analizi birleşik konveksiyon-difüzyon denklemi çözülerek yapılmaktadır. Nümerik simülasyonlar yapılırken sonlu elemanlar yöntemi kullanılmaktadır. Giriş debisi, kardiyak döngünün cihaz üzerindeki etkisini simule etmek için sinüzoidal dalga fonksiyonuyla modellenmektedir. Model ilk olarak hem durağan durumun deneysel sonuçlarlarla hem de geçici rejim analizinin korelasyonlarla karşılaştırılmasıyla doğrulanmaktadır. Doğrulanan model, hem durağan akış hem de pulsatil akış durumlarında parametrik çalışma için kullanılmaktadır. Sonuçlar, artan boy-en oranının, yakınsayan gaz transfer hızına, artan basınç kaybına, ve artan duvar kayma gerilimine sebep olduğunu göstermektedir. Biyouyumluluk için uygun kayma gerilimi limitlerinin sağlanması kritik bir rol oynamaktadır. Ayrıca, durağan durum analizinin yüksek boy-en oranları için gaz transfer performansını daha düşük bulduğu gözlemlenmektedir. Newtonyen modelde basınç kaybı ve kayma gerilimi değerlerinin Carreau modele göre daha düşük olduğu görülmüştür. Buna karşılık, Newtonyen modelde gas transfer performansının Carreau model sonuçlarına göre yaklaşık % 5 daha yüksek olduğu bulunmaktadır.

TABLE OF CONTENTS

ACKNOWLEDGEMENTS iii
ABSTRACT iv
ÖZET v
LIST OF FIGURES viii
LIST OF TABLES xi
LIST OF SYMBOLS xiii
LIST OF ACRONYMS/ABBREVIATIONS xv
1. INTRODUCTION 1
  1.1. Newtonian Modelling of Blood 3
  1.2. Non-newtonian Modelling of Blood 4
  1.3. Literature Survey 6
  1.4. Scope of the Thesis 8
  1.5. Thesis Layout 9
2. MATHEMATICAL FORMULATION 10
3. NUMERICAL METHOD 15
4. TESTS AND VALIDATIONS 17
  4.1. Steady-State Analysis 17
    4.1.1. Newtonian Model 17
    4.1.2. Carreau Model 20
  4.2. Transient Analysis 24
5. RESULTS AND DISCUSSION 28
  5.1. Newtonian Case 28
    5.1.1. Flow Results 28
    5.1.2. Pressure Drop Results 30
    5.1.3. Gas Transfer Results 31
    5.1.4. Shear Stress Results 35
    5.1.5. Newtonian Results Evaluation and Discussion 38
  5.2. Non-Newtonian Case and Comparison with Newtonian Results 41

    5.2.1. Flow Analysis 41
    5.2.2. Pressure Drop Analysis 44
    5.2.3. Gas Transfer Analysis 45
    5.2.4. Shear Stress 47
    5.2.5. Non-Newtonian Results Evaluation and Discussion 48
6. CONCLUSION 53
REFERENCES 55

LIST OF FIGURES

Figure 1.1. ECMO device schematic view. 2

Figure 2.1. Micro-oxygenator. 11

Figure 2.2. Fiber bundles in micro-oxygenator. 12

Figure 2.3. The oxygen dissociation curve in blood (ODC). 14

Figure 3.1. An example of the mesh structure. 16

Figure 4.1. Horizontal velocity profile at the middle section of the channel for $Q_0 = 90\ mL/h$. 18

Figure 4.2. Average oxygen saturation (sO_2) at the outlet for $Q_0 = 90\ ml/h$. . . 19

Figure 4.3. Mesh convergence of Carreau model for average oxygen saturation (sO_2) at the outlet for $Q_0 = 90\ ml/h$. 20

Figure 4.4. Comparing oxygen transfer rates for validation. 22

Figure 4.5. Average oxygen saturation in blood at the outlet for T=0-17. . . . 24

Figure 4.6. Sherwood number comparison of the correlation and the numerical results. 27

Figure 5.1. Velocity contours for (a) AR=60/2, (b) AR=40/3, (c) AR=20/6, and (d) AR=10/12 at peak pulsation in m/s. 29

Figure 5.2. Flow streamlines at peak pulsation for (a) AR=60/2, (b) AR=40/3, (c) AR=20/6, and (d) AR=10/12. 30

Figure 5.3. Local flux magnitude around the chosen membrane for all configurations. 32

Figure 5.4. Concentration distribution at peak pulsation for (a) AR=60/2, (b) AR=40/3, (c) AR=20/6, and (d) AR=10/12. 33

Figure 5.5. Oxygen transfer rates for the last period. 34

Figure 5.6. Shear stress distribution in Pa around maximum value in the domain at peak pulsation. 36

Figure 5.7. Maximum WSS for each configuration. 37

Figure 5.8. Average saturation in the section lines between columns. 38

Figure 5.9. Total oxygen transfer rate of columns for each configuration. . . . 39

Figure 5.10. Time-averaged outlet saturation vs. aspect ratio. 40

Figure 5.11. Velocity contours for (a) AR=40/3, (b) AR=30/4, (c) AR=24/5, and (d) AR=20/6 at peak pulsation in m/s. 42

Figure 5.12. Shear rate vs. viscosity for Carreau and Newtonian model. 42

Figure 5.13. Average shear rates throughout the channel for different configurations. 43

Figure 5.14. Oxygen transfer rates of the Carreau model for different configurations. 45

Figure 5.15. Local flux magnitude around the same membrane for all configurations. 46

Figure 5.16. Maximum WSS values vs. time for different configurations. 47

Figure 5.17. Time-averaged outlet saturation vs. aspect ratio for the Carreau model. 49

Figure 5.18. Average saturation in the section lines between columns for Carreau model. 50

Figure 5.19. Total oxygen transfer rate of columns for Carreau model. 51

LIST OF TABLES

Table 4.1. Mean percentile differences between meshes for velocity profile at the middle section. 19

Table 4.2. Percentile differences between consecutive meshes for oxygen saturation at the outlet. 20

Table 4.3. Oxygen transfer rates in mL/h and relative errors. 23

Table 5.1. Pressure drop at peak pulsation and normalized drag for all configurations. 31

Table 5.2. Pressure drop and normalized drag comparison of all configurations in steady-state. 31

Table 5.3. Time-averaged oxygen saturation level at the outlet for the last period. 34

Table 5.4. Saturation and oxygen transfer rate comparison of all configurations in steady-state. 35

Table 5.5. Maximum and minimum WSS comparison for all configurations in steady-state. 37

Table 5.6. Pressure drops for the best alternatives. 41

Table 5.7. Pressure drop at peak pulsation and normalized drag for all configurations in Carreau model. 44

Table 5.8. Oxygen transfer rates for the Newtonian and the Carreau models. 46

Table 5.9. Max WSS values comparison for Newtonian and Carreau models. . 48

Table 5.10. Pressure drops for the best alternatives. 52

LIST OF SYMBOLS

A	Pulsation Amplitude
$A_{interface}$	Area of the Fiber-Blood Interface
c	Concentration
$c_{\text{interface}}$	Concentration at the Fiber-Blood Interface
c_{inlet}	Concentration at the Channel Inlet
D	Fiber Diameter
D_c	Diffusion Coefficient of the Species in the Interstitial Region
E	Strain Rate Tensor
$\bar{F}_D$	Normalized Drag per Unit Length
F_D	Drag Force
h	Convective Mass Transfer Coefficient
HR	Heart Rate
j	Molar Flux at the Fiber-Blood Interface
L	Characteristic Length
n	Power-Law Index
p	Fluid Pressure
Q_0	Mean Blood Flow Rate
R	Reaction Term
Re	Reynolds Number
Sc	Schmidt Number
Sh	Sherwood Number
sO_2	Oxygen Saturation
T	Period of Device Cycle
t'	Time in Period
U	Inlet Velocity
$\mathbf{v}$	Velocity Field
Wo	Womersley Number

β	Blockage Ratio
$\dot{\gamma}$	Shear Rate
λ	Time Constant for Carreau Model
μ	Dynamic Viscosity
μ_0	Zero Shear Rate Viscosity
μ_∞	Infinite Shear Rate Viscosity
ν	Kinematic Viscosity
$\mathit{\Pi}$	Second Invariant of the Strain Rate Tensor
ρ	Density
τ	Extra Stress Tensor
ϕ	Angular Position on Membrane
ω	Angular Oscillation Frequency

LIST OF ACRONYMS/ABBREVIATIONS

2D	Two Dimensional
3D	Three Dimensional
AR	Aspect Ratio
BDF	Backward Differentiation Formula
CFD	Computational Fluid Dynamics
EC	Endothelial Cell
ECMO	Extracorporeal Membrane Oxygenators
MUMPS	Multifrontal Massively Parallel Sparse Direct Solver
ODC	Oxygen Dissociation Curve
RBC	Red Blood Cell
WSS	Wall Shear Stress

1. INTRODUCTION

Chronic obstructive pulmonary disease has increased significantly in recent years and become the third leading cause of death worldwide [1] and it is expected to be the leading cause of death in 2030 [2]. People with this disease suffer from shortness of breath due to poor pulmonary oxygen transfer to the blood and carbon dioxide elimination from the blood, leading to death if not intervened. In some cases, the desired improvement cannot be achieved despite noninvasive ventilation. Most patients with congenital cystic fibrosis, need long-term and continuous oxygen support. Organ transplantation required for these patients is not always possible due to limited donors and time. Therefore, there is a great need for a permanent implantable lung support system.

By performing complete or partial function of the lung, the extracorporeal membrane oxygenator (ECMO) system gives the patient life support. The patient is temporarily supported by ECMO equipment. When conventional treatments fail, ECMO is utilized. Lung illness cannot be cured with ECMO devices. It merely gives the patient's lungs time to recover. Unoxygenated blood is drawn from a vein by the ECMO pump, which then pumps the blood into the oxygenator or artificial lung. Here, oxygen is provided and carbon dioxide from the blood is eliminated. Because dark blood deficient in oxygen turns bright red when oxygen is introduced, a color change occurs. In Figure 1.1, schematic view of an ECMO device is shown.

Although ECMO devices are mostly used in critical care situations, such as severe respiratory failure, cardiac failure, or during heart surgery, as actual lung support systems, microfluidic artificial lungs are studied intensively by many scientists due to the advantages they promise such as targeted and controlled oxygenation process and the potential for miniaturization making them less invasive and possibly wearable in the future.

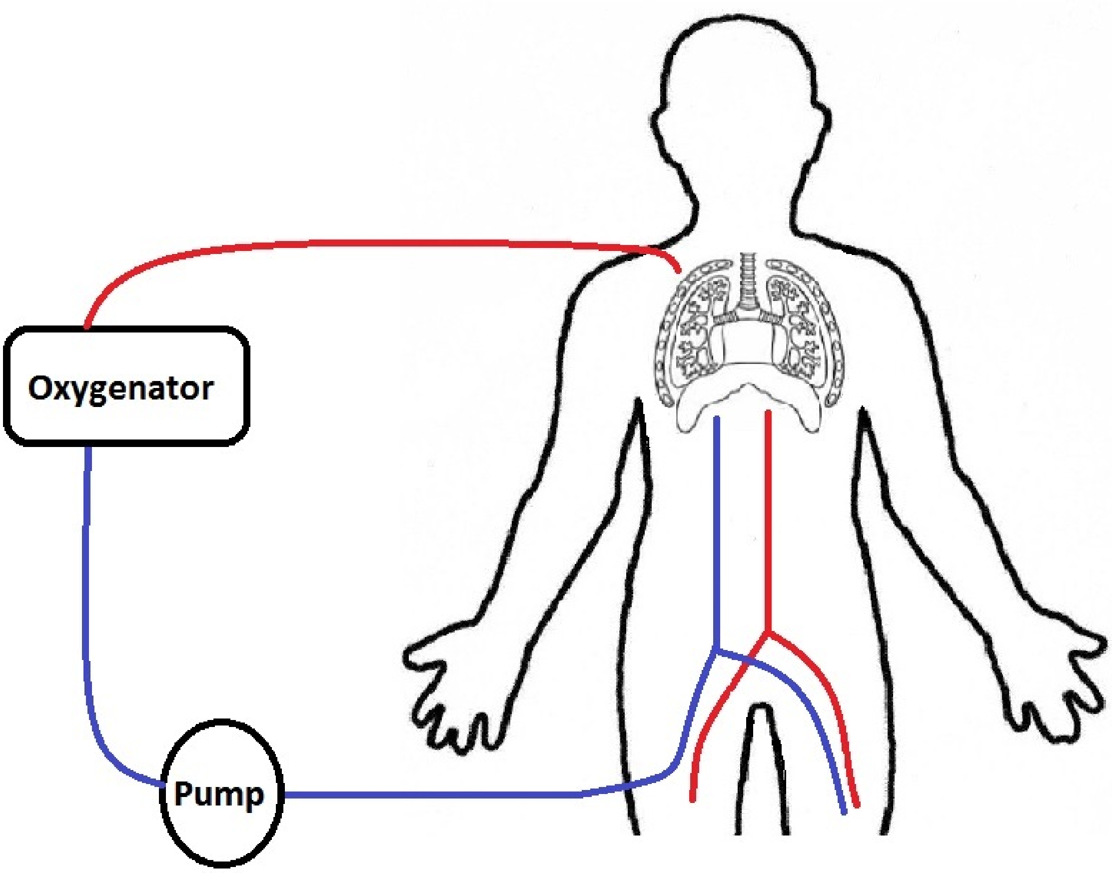

Figure 1.1. ECMO device schematic view.

Lung support systems simply consist of the blood pump, the oxygenator module, and the main channel through which blood flow occurs. The hollow fiber bundles in the oxygenator module are surrounded by specialized membranes and oxygen diffuses through these bundles. These membranes are covered with an anti-thrombogen coating that prevents the passage of thrombogen from the blood to the fibers. The blood flows around the fiber bundles in the main channel. Hemoglobin in the blood binds to the oxygen molecules that pass from the fiber bundle to the blood through the membrane at the blood-fiber interface. Depending on the cause and level of the oxygen transfer malfunction, the blood flow in the main channel can be created passively, either by a pump connected to the patient's venous vascular system or, less commonly, by connecting the artificial lung directly to the patient's arterial system [3]. While the flow is steady in the systems using a pump, it is pulsatile for the systems driven by the cardiac-cycle.

Microfluidic artificial lungs promise to reduce the need for transverse mixing using small blood side channels, resulting in efficient, compact artificial lung devices with very low pressure drops [4]. Another advantage of microfluidic oxygenators is that the ratio of exchange-surface-area to blood volume increases as the channel gets smaller. Furthermore, implementing biomimetic flow routes in which blood cells are exposed to pressures, flow velocities, and shear stresses similar to those found in real vasculature would be useful in the long run [5]. Moreover, the option to use pure oxygen for the oxygen side as sweeping gas can greatly enhance the saturation rates making the device more efficient.

Despite the many advantages they offer, microfluidic artificial lungs are still not available to patients. The most important reason for this is that they are not yet biocompatible. Exposure to different shear stresses during blood flow causes some undesirable reactions. In order to prevent this, studies are carried out in the field of biomaterials in different applications. Biomaterials are significantly improved for use in other applications, such as stents, etc., particularly in terms of their anti-thrombogenic characteristics. However, the development of hemocompatible materials for microfluidic artificial lungs does not proceed at the same rate [6].

The design of these devices involves complex fluid mechanics, which can be effectively studied through the use of computational fluid dynamics (CFD) models. CFD models allow for the simulation of blood flow and gas exchange in microchannels, and the evaluation of the performance of artificial lungs under different conditions. There are different types of models used in blood flow simulation, including Newtonian and non-Newtonian models. It is of great importance to understand the underlying mechanisms of different models and their applications in microfluidic artificial lung design.

1.1. Newtonian Modelling of Blood

Newtonian blood flow modeling is a type of CFD model that assumes blood to be a homogeneous, isotropic, and Newtonian fluid. This means that the blood behaves as a simple fluid, following the principles of Newtonian mechanics, such as viscosity being constant and independent of the rate of deformation. In this model, blood viscosity is a constant parameter, and the fluid mechanics of blood flow are described by the Navier-Stokes equations, which govern the motion of a viscous fluid.

The Newtonian model is often used in blood flow modeling because it is relatively simple and computationally efficient. It is well-suited for studying large-scale hemodynamic phenomena, such as blood flow in major vessels, where the flow is typically laminar and the shear rates are low. However, the Newtonian model is less accurate in modeling the behavior of blood in microcirculation and in regions of disturbed flow, such as stenotic or bifurcating vessels, where the flow is complex and non-Newtonian effects become significant.

Overall, the Newtonian model provides a good approximation of blood flow in many physiological conditions and is a valuable tool for studying cardiovascular diseases. However, in certain situations, such as in microfluidic artificial lungs where blood is exposed to high shear rates, non-Newtonian models may provide a more accurate representation of blood behavior.

1.2. Non-newtonian Modelling of Blood

There are several non-Newtonian models used for blood flow modeling, including the Power-Law, Carreau, Casson, Carreau-Yasuda, and Herschel-Bulkley models. Here are some brief explanations of these models and their advantages and disadvantages:

Power-law model: The power-law model assumes that the relationship between shear stress and shear rate is a power law function. This model is widely used in blood flow simulations and can account for both shear-thinning and -thickening behavior of blood. The advantages of the power-law model are its simplicity, versatility, and ability to fit experimental data well. However, the model has limited accuracy in predicting the flow behavior of blood in complex geometries and under extreme flow conditions.

Casson model: The Casson model assumes that blood behaves as a Bingham fluid, which means that it has a yield stress and requires a certain amount of shear stress to initiate flow. This model can accurately capture the flow behavior of blood in stenotic vessels and other complex geometries. However, the Casson model is computationally expensive and requires accurate measurements of yield stress and viscosity.

Carreau-Yasuda model: The Carreau-Yasuda model assumes that blood viscosity is a function of shear rate and temperature. This model can accurately capture the rheological behavior of blood under different flow conditions, including shear thinning and thickening. The advantages of the Carreau-Yasuda model are its accuracy and versatility. However, the model requires accurate measurements of several rheological parameters, which can be difficult to obtain experimentally.

Herschel-Bulkley model: The Herschel-Bulkley model is similar to the Casson model but assumes that blood has a power-law relationship between stress and strain rate above a certain yield stress. This model can accurately capture the flow behavior of blood in stenotic vessels and other complex geometries. However, the model requires accurate measurements of yield stress and viscosity and is computationally expensive.

Carreau Model: The Carreau model is similar to the Carreau-Yasuda model but assumes that the viscosity of blood varies as a function of both shear rate and time. This model can accurately capture the rheological behavior of blood under different flow conditions, including shear thinning and thickening. The advantages of the Carreau model are its accuracy and ability to fit experimental data well. However, like the Carreau-Yasuda model, it also requires accurate measurements of several rheological parameters, which can be challenging to obtain experimentally.

In this study, the Carreau model is chosen for modeling blood since it is accurate, the required parameteres are already obtained experimentally, and also it is frequently used in the literature.

1.3. Literature Survey

Latest research studies mainly focus on enhancing gas transfer efficiency, providing a biocompatible design, and achieving a low pressure drop.

Chan *et al.* [7] investigated numerically gas transport in a cardiac-driven artificial lung for pulsatile flow using a Newtonian fluid. The investigated parameters are gas transfer rate and pressure drop as a function of geometry, Reynolds number, and oscillation frequency. The study favors staggered array configuration with a high oscillation frequency, high Reynolds number, and low void fraction of the fiber bundle for an efficient gas transfer rate. It is indicated that for most cases, high pressure drops accompany high gas transfer rates.The study found that a staggered array configuration with high oscillation frequency, high Reynolds number, and low void fraction of the fiber bundle resulted in an efficient gas transfer rate. Compared to the inline square array configuration, the staggered array configuration showed a 20% in Sherwood number for Re=1, 49% increase for Re=5, and 82% increase for Re=10, with an oscillation frequency of 1, wave amplitude of 0.5, and void fraction of 0.8036. The pressure drop in a unit length was also lower in the staggered array configuration except for low void fraction values.

Taskin *et al.* [8] modeled the flow and oxygen transfer in a 2-D oxygenator for a non-Newtonian fluid. The model used a “two-region” approach to create the domain and implemented seperate diffusion processes for blood and hollow-fiber regions separately. As a result of this, the model includes the membrane resistance effect leading to oxygen partial pressures variation along the fiber-blood interface. The study showed that analyses including separate hollow-fiber modeling provided more accurate results for geometries with dense packings.

Gage *et al.* [9] studied the pressure drop for a membrane oxygenator using CFD along with an experimental setup. The numerical model solves the Navier-Stokes Equations in 3-D for a Newtonian fluid with a source term to account for losses using a Darcian porous media model. The results indicate a good agreement between numerical and experimental findings for the blood flow rate of 2 L/min. However, the numerical simulations underestimate the pressure drop for the blood flow rates of 4 L/min and 6 L/min.

Dierickx *et al.* [10] investigated the effects of fiber alignments –inline square, staggered square, and equilateral triangle- on the hydrodynamics of an artificial lung. The numerical study is done in 2-D by using both Newtonian and non-Newtonian Casson models and the differences are compared. The study finds out that equilateral triangle generates less resistance and resistance increases as the porosity decreases. In the context of the shear-thinning Casson viscosity model, the flow behavior exhibits a noticeable reduction at low Reynolds numbers in both velocity gradients and shear rates, leading to an elevation in local fluid viscosity. Consequently, this higher viscosity results in an increased resistance to flow. However, at high Reynolds numbers, there is no discernible disparity between the flow properties of Newtonian and non-Newtonian blood, owing to the higher shear rates prevalent in the system.

Hormes *et al.* [11] examined a hollow-fiber oxygenator to predict oxygen and carbon dioxide transfer rates. The numerical study is conducted with a modified CFD model that takes into account the physical solubility and the chemical bond of oxygen and carbon dioxide in order to predict better the overall diffusivity. The blood was modeled using a non-Newtonian fluid model, namely the model of Ballyk. The model is validated with an experimental setup for different mass flow rates. The mass flow rates and oxygen partial pressures are compared to analytical solutions. They are in better agreement with experiments when constant inlet partial pressure boundary condition is applied.

Kaesler *et al.* [12] investigated the oxygen transfer in a microfluidic artificial lung for steady state condition under Newtonian flow assumption with both a 2-D CFD model and an experimental setup. The study focuses on the comparison of gas transfer performances with correlation models for varying inlet volumetric flow rates. The

CFD model includes separate modelling of plasma and red blood cells along with a reaction of oxygen and hemoglobin to form oxyhemoglobin. The results show that although correlation models give accurate results for specific inlet conditions, they lack of covering varying inlet volumetric flow rates with consistent accuracy.

1.4. Scope of the Thesis

Previous studies in the literature mainly focused on modeling and maximizing gas transfer in steady flows [8,11], or comparing gas transfer efficiency for inline square and staggered arrays in pulsatile flow [7]. In classical flow around a cylinder array type of problems, the column to row ratio is known to have an important effect of the flow structure and properties. Also, biocompatibility aspects need to be taken into account in artificial lung design.

In the present study, we consider a microfluidic artificial lung consisting of fiber bundles arranged in a staggered manner relative to each other with different column to row ratios, namely the aspect ratios. By considering the pulsatile flow characteristics, efficient biocompatible fiber configuration conditions are determined and the differences with the steady case are also revealed. The geometric parameters of the micro-oxygenator, i.e. the numbers of fiber bundles rows and columns, are adjusted to promote device safety by creating a biocompatible flow path for the blood, in addition to lowering pressure drop and improving gas transfer efficiency. Blood-surface interactions within the device have also an impact on safety and biocompatibility. The primary reason why microfluidic artificial lung devices are not yet biocompatible is the formation of high or low speed zones and stagnant areas in the blood flow path along hollow fiber membranes. This is strongly related to shear stress levels imposed on Endothelial Cell (EC) coatings. It has long been known that coating blood flow routes with human endothelial cells reduces the risk of clotting, giving the endothelium the potential to prevent coagulation and thrombus formation [13]. In order to further improve the function and durability of the EC coating, the wall shear stress (WSS) levels applied to endothelial cells must be kept within acceptable limits. Also, the limited space required for the integration of the device into the body necessitates a more efficient gas transfer in a small volume. Additionally, a design is required within the pressure drop values allowed by the cardiac-cycle. The effect of aspect ratio on these three mentioned output parameters is investigated in the context of staggered array design and different configurations are compared with each other in this study, for both steady and pulsatile conditions. Using the same geometries and conditions, blood flow is analyzed with both the Newtonian model and the Non-Newtonian Carreau model. The effects of these two different models on the output parameters are investigated.

1.5. Thesis Layout

In the following chapter of this thesis, the mathematical formulations for the flow and transport analysis are given. The geometry and boundary conditions are described in detail. In Chapter 3, the applied numerical method is explained, as well as information on the mesh structure and the time integration is provided. In Chapter 4, the steady-state case solutions are first validated with the results of an experimental study in the literature, with the same geometry and boundary conditions. Then, for the pulsatile case, a validation study is conducted using existing correlations in the literature for dimensionless parameters such as normalized drag and Sherwood number. In Chapter 5, the results for both Newtonian and Non-Newtonain Carreau models are displayed and evaluated in terms of flow analysis, gas transfer characteristics, pressure drop, and biocompatibility. The findings are summarized in Chapter 6.

2. MATHEMATICAL FORMULATION

The oxygen concentration and gas exchange rate in the fiber oxygenator are obtained by solving the combined mass transfer equation. Oxygen transfer in the main channel is governed by a convection-diffusion equation and expressed as

$$\frac{\partial c}{\partial t} = \nabla \cdot (D_c \nabla c) - \nabla \cdot (\mathbf{v} c), \tag{2.1}$$

where c is the oxygen concentration, $\mathbf{v}$ is the velocity field that the species are moving with, and D_c is the diffusion coefficient of the species in the interstitial region. The diffusion coefficient of oxygen in the blood is taken as 1.62×10^{-5} cm^2/sec which is obtained from experimental studies for normal human blood at 37°C and at average 42% hematocrit level [14].

The flow field of the blood in the interstitial space between the fibers is obtained using the incompressible mass and momentum conservation equations. Mass conservation equation, in other words continuity equation, is expressed as

$$\nabla \cdot \mathbf{v} = 0, \tag{2.2}$$

and the momentum conservation equation is expressed as

$$\rho(\frac{\partial \mathbf{v}}{\partial t} + \mathbf{v} \cdot \nabla \mathbf{v}) = -\nabla \mathrm{p} + \nabla \cdot \tau, \tag{2.3}$$

where ρ describes the density, p is the fluid pressure, and τ is the extra stress tensor.

The extra stress tensor τ is expressed in Newtonian model formulation. The blood is assumed to have a constant viscosity μ in Newtonian formulation for all shear rates which is valid for shear rates higher than 100 s^{-1} [15]. The extra stress tensor is obtained by $\tau = 2\mu \mathrm{E}$ for Newtonian fluids with E being the strain rate tensor expressed as $\mathrm{E} = \frac{1}{2}\left(\nabla v + (\nabla v)^T\right)$.

The non-Newtonian Carreau model is used to model shear thinning effects of blood. This model is especially useful to exhibit high viscosity values for low shear rates which is the observed case with blood in experiments. Besides, the blood has constant low viscosity values for high shear rates. Thus, the model has two parameters, namely zero shear rate and infinite shear rate viscosities, μ_0 and μ_∞ respectively. These two parameters represent viscosity values at low and high shear rates. Then, the extra stress tensor for Carreau model is written as

$$\tau = \left\{\mu_\infty + (\mu_0 - \mu_\infty)\left[1 + (\dot{\gamma}\lambda)^2\right]^{\frac{n-1}{2}}\right\}\left[\nabla v + (\nabla v)^T\right], \tag{2.4}$$

where $\dot{\gamma} = \sqrt{\frac{1}{2}\mathit{\Pi}}$. In this equation, $\mathit{\Pi}$ is the second invariant of the strain rate tensor and λ is the time constant. Carreau model parameters are found by rheological experimental studies as $\mu_\infty = 3.45$ mPa.s, $\mu_0 = 56$ mPa.s, $\lambda = 3.313$ s, and $n = 0.3568$ being Power-Law index [16].

The flow is found to be laminar in the interstitial region for the considered Reynolds number defined as $Re = \rho U\mathrm{D}/\mu$, with the bundle diameter D and the inlet velocity U.

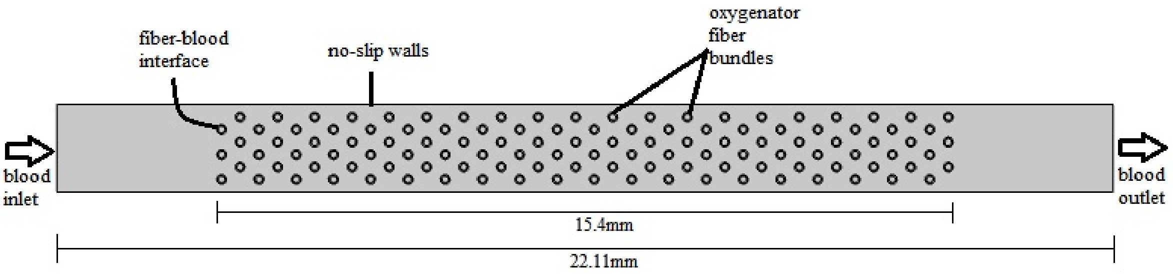

Figure 2.1. Micro-oxygenator.

An example of micro-oxygenator geometry is given in Figure 2.1. The main channel through which the blood flow takes place has a cross section of 1.82×1.82 mm^2 and a length of 22.11 mm.

Blood flows perpendicularly through fibers configured in different aspect ratios. The aspect ratio is determined to be the ratio of the number of columns to the number of rows. The fiber bundles are arranged in a staggered manner relative to each other in each row. Staggered fiber configuration has been shown to perform a better oxygen transfer in former studies [7, 17].

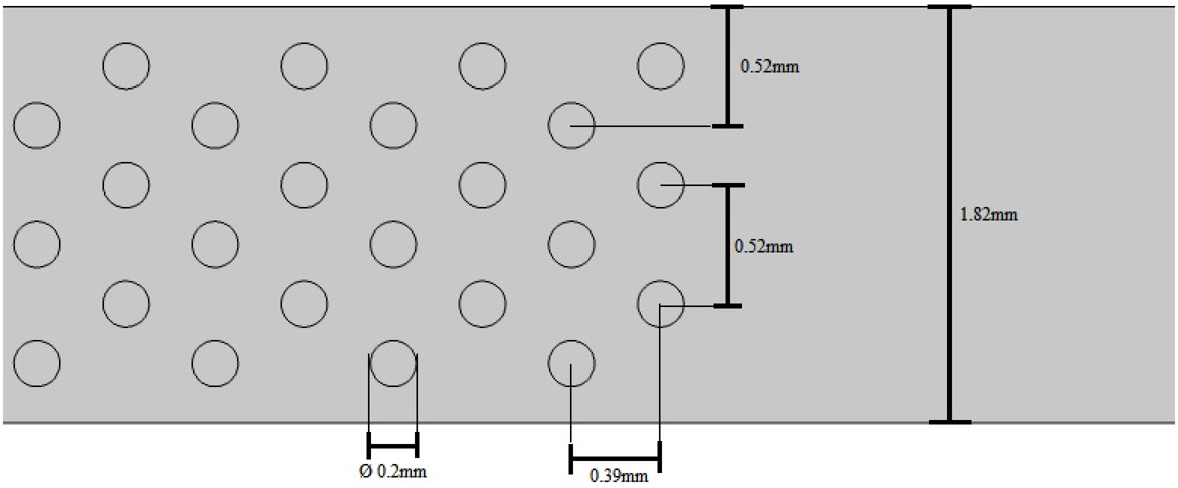

Figure 2.2. Fiber bundles in micro-oxygenator.

The outer diameter of the fiber bundles is 0.2 mm as given in Figure 2.2. For ease of analysis, the geometry of the micro-oxygenator has been simplified in 2D. Due to the laminar flow conditions in the main channel and all of the fibers being unidirectional and perpendicular to the flow, the 2D flow assumption is a suitable approach [12].

Inlet boundary condition is applied on the left side of the oxygenator with 3 different blood flow rates of 20 ml/h, 50 ml/h, and 90 ml/h for the steady-state case. For the transient case, a sinusoidal flow rate is applied at the left boundary to investigate the pulsatility effects. This sinusoidal flow rate function is to simulate the right ventricular flow entering the main channel after passing through a compliance chamber that partially attenuates the flow rate. This flow rate function can be written as

$$Q'_{\text{puls}} = Q_0\left(1 + \mathrm{A}\sin\left(\omega t'\right)\right) \qquad \text{for } 0 \le t' \le \frac{2\pi}{\omega}, \tag{2.5}$$

where Q_0 is the mean blood flow rate which is 90ml/h, A is the pulsation amplitude which is 0.5, and t' denotes the time. The angular oscillation frequency ω is given by

$$\omega = 2\pi(HR) = 439.82 min^{-1}, \tag{2.6}$$

where HR is the heart rate and chosen as 70 bpm considering a value for an average human in normal conditions [18]. Then, the Womersley number Wo becomes

$$Wo = \mathrm{D}\sqrt{\frac{\omega\rho}{\mu}} = 0.29808. \tag{2.7}$$

The outlet boundary condition is applied on the right side with a constant pressure. No-slip velocity condition is imposed on the top and bottom channel walls, as well as on the blood-fiber interface consisting of fiber bundle walls.

For the transport equation, oxygen concentration constraints are set to represent the oxygen inflows from both the blood inlet section and the fiber-blood interface. To evaluate the oxygen concentration for inflow boundaries, several factors should be taken into account: oxygen molecules' partial pressure, hemoglobin concentration, and hemoglobin's oxygen-carrying capacity. The oxygen saturation ratio, which corresponds to the oxygen partial pressure in the fiber-blood interface, is obtained by using the oxygen dissociation curve in blood. To make use of the saturation ratio, the maximum oxygen carrying capacity of the blood must be known. The maximum volume of oxygen which can be carried by the blood when it is fully saturated is 21 mL of oxygen per 100 mL of blood with a normal hemoglobin concentration. Only the oxygen molecules carried by hemoglobin are utilized for the transport mechanism. However, a negligibly small part of this 21 mL oxygen is not carried by hemoglobin; instead, it dissolves in simple solution which corresponds to the blood plasma. Therefore, in this study, it is assumed that all of the oxygen molecules in the blood are chemically bound to hemoglobin molecules in the red blood cells.

Based on the ODC given in Figure 2.3 and considering the oxygen partial pressures, the oxygen saturation rates at the blood inlet boundary and fiber-blood interface are determined [19]. At the blood inlet section, the oxygen saturation is set to 69% corresponding to the oxygen partial pressure of 40.2 mmHg. At the outlet, there is an outflow condition for the oxygen which specifies the normal derivative of the concentration as zero. Since the concentration is dominated by streamwise convection, streamwise diffusion may be neglected. This is valid for large Schmidt number problems, where it is a dimensionless number defined as the ratio of momentum diffusivity (viscosity) to mass diffusivity.

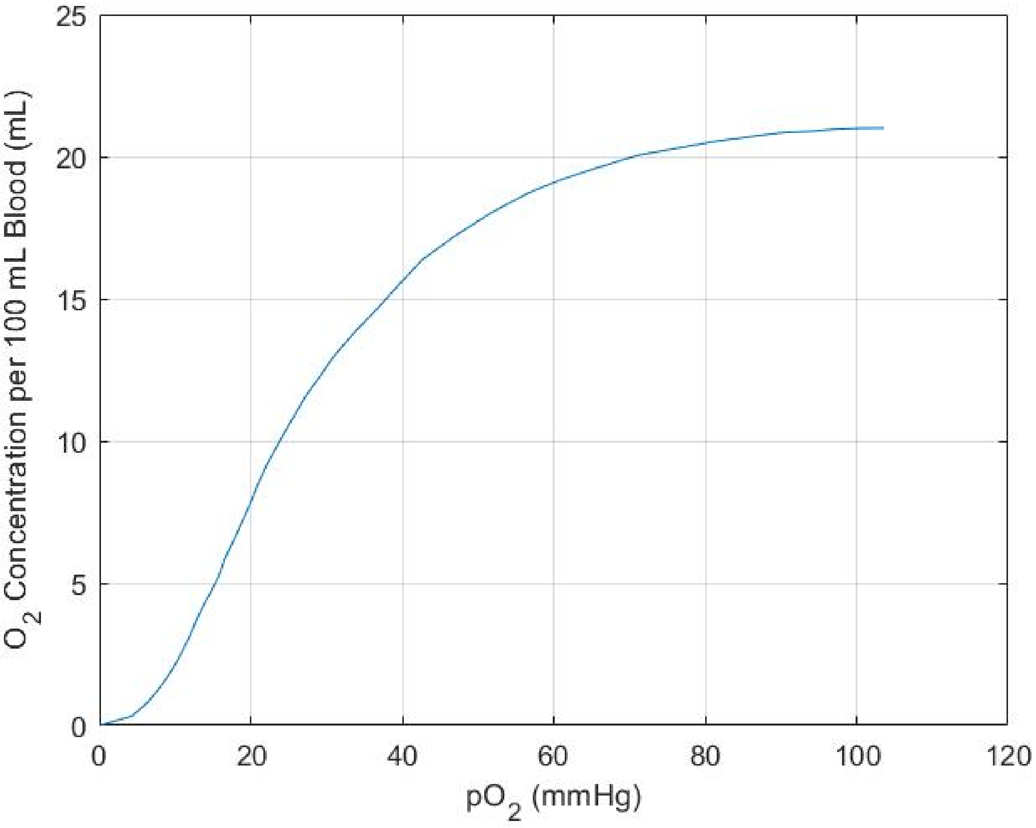

Figure 2.3. The oxygen dissociation curve in blood (ODC).

The oxygen concentration at the interface between the fiber and blood is maintained at 100% oxygen saturation. This is attributed to the negligible mass transfer resistance across the fiber membrane, implying that the oxygen concentration at the surface of the fiber corresponds to that within the fibers which is fully saturated [20]. The concentration values corresponding to these saturation levels are obtained in mole/liters by using the ideal gas law for oxygen. Thus, the molar concentration is equal to 5.3414 mol/m^3 at the blood inlet and 7.7411 mol/m^3 at the fiber-blood interface.

3. NUMERICAL METHOD

Numerical simulations are performed using commercial software COMSOL Multiphysics based on the finite element method. The main equations for the fluid and transport problems mentioned above are segregated and non-linear. The convection term in the transport equation depends on the velocity field obtained from the momentum equation. For the solution of the discrete equation system in space, MUMPS-based direct solver (Multifrontal Massively Parallel sparse direct Solver) is used instead of the more time-consuming iterative approach. The typical simulation takes 850 CPU hours with Intel Xeon W–2155 processor. The momentum equation is solved first and then the transport equation is solved using the velocity field obtained from the momentum equation.

Both linear and quadratic interpolation functions have been tried for the velocity and concentration variables in terms of the desired convergence and computational cost. Finally, linear interpolation functions are used for the velocity and pressure, and quadratic interpolation functions are used for the concentration.

The Anderson acceleration stabilization technique, which is a nonlinear convergence acceleration method that uses information from previous Newton iterations, is applied for the transport equation to reduce the computation time.

Newton's method with constant damping factor is chosen as the nonlinear solver. The absolute tolerance is set to be less than 10^{-6} as the convergence criterion for all variables.

For time integration, the adaptive and implicit Backward Differentiation Formulas (BDF) method is used. The maximum time step is determined as a reference for the adaptive time-stepping algorithm following trials by gradually decreasing it for computational cost and is set to be of the order of $10^{-4}s$.

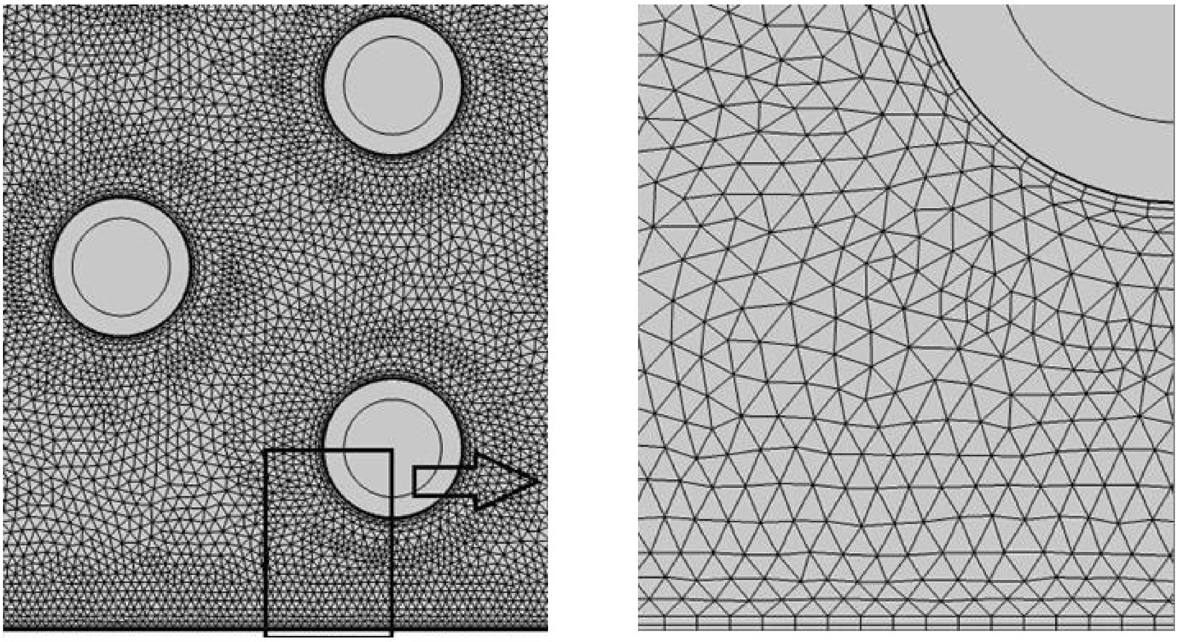

Figure 3.1. An example of the mesh structure.

For the space discretization, triangular mesh elements are implemented throughout the domain except for the immediate periphery of the membrane and the channel walls where quadrilateral mesh elements are used. An example mesh structure near the walls and quadrilateral mesh elements that are used in boundary layers are shown in Figure 3.1.

4. TESTS AND VALIDATIONS

The tests and validation section consists of two parts, where Newtonian and Carreau models are separately validated for steady-state analysis, and only the Newtonian model is validated for transient analysis. Since empirical correlations in the literature for transient analysis are based on the Newtonian case, transient case is only validated for Newtonian model.

4.1. Steady-State Analysis

4.1.1. Newtonian Model

Before the numerical analysis, a mesh convergence study is performed to show that the results are independent of the mesh structure. For this reason, the geometry with AR=40/3 is chosen and 6 different mesh structures with increasing number of mesh elements are created for the steady-state case.

In order to compare the results of different meshes, the selected parameters are examined by cross-sectioning the middle part of the main channel and the outlet. These parameters are the horizontal velocity profile in the middle section for flow analysis verification and the oxygen saturation ratio at the outlet for transport analysis verification.

As seen in Figure 4.1, the velocity profiles converge gradually from the first mesh (Mesh 1) with total element number of 83,264 to the sixth mesh structure (Mesh 6) with total element number of 660,784. The number of mesh elements at each intermediate level and their horizontal velocity profiles at the middle section can be observed from the figure.

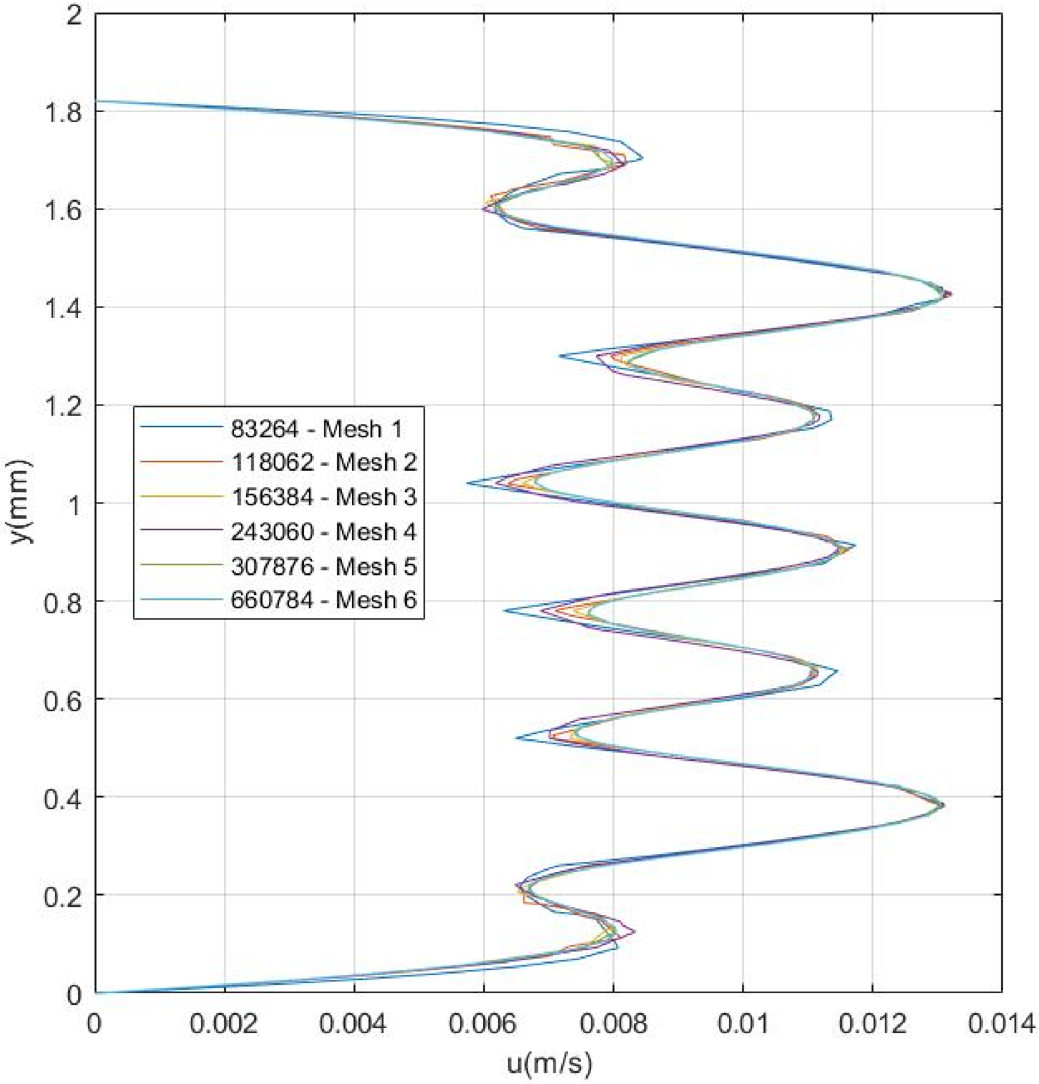

Figure 4.1. Horizontal velocity profile at the middle section of the channel for $Q_0 = 90\ mL/h$.

The effect of the mesh number is particularly evident in the local minimum and maximum points of the horizontal velocity profile due to the velocity fluctuations in the section between two columns of cylinders.

Mean percentile differences for velocity profiles are calculated regarding the average of horizontal velocity differences. For the meshes with less nodes, extra points to be compared are generated using interpolated data. The average of percentile differences between consecutive meshes are shown in Table 4.1.

Table 4.1. Mean percentile differences between meshes for velocity profile at the middle section.

	Mesh 1-2	**Mesh 2-3**	**Mesh 3-4**	**Mesh 4-5**	**Mesh 5-6**
Percentile Difference	5.58%	2.78%	2.51%	1.36%	0.49%

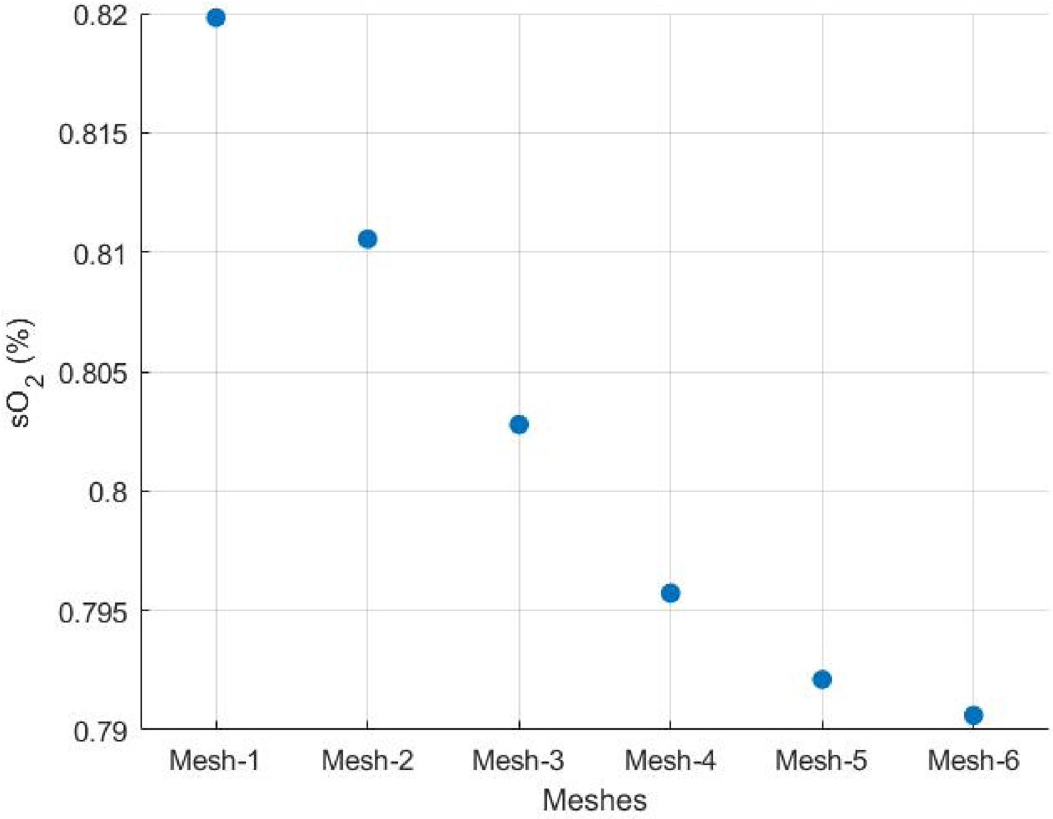

Figure 4.2. Average oxygen saturation (sO_2) at the outlet for $Q_0 = 90\ ml/h$.

The average oxygen saturation at the outlet is presented for different meshes in Figure 4.2. Percentile differences between consecutive meshes are given in Table 4.2 for the oxygen saturation at the outlet. The average saturation values are calculated for each mesh structure, and then the percentile errors are obtained for consecutive meshes. Figure 4.2, Table 4.1, and Table 4.2 show that Mesh-5 converges to Mesh-6, hence Mesh-6 is chosen for subsequent analysis.

Table 4.2. Percentile differences between consecutive meshes for oxygen saturation at the outlet.

	Mesh 1-2	**Mesh 2-3**	**Mesh 3-4**	**Mesh 4-5**	**Mesh 5-6**
Percentile Difference	0.78%	0.84%	0.89%	0.46%	0.19%

4.1.2. Carreau Model

For the mesh independence of the Carreau Model, the same mesh structures are used. However the results are not converged within desired tolerance. Additional two mesh structures are created to obtain better mesh independence. The results of different meshes converge gradually as can be seen in Figure 4.3.

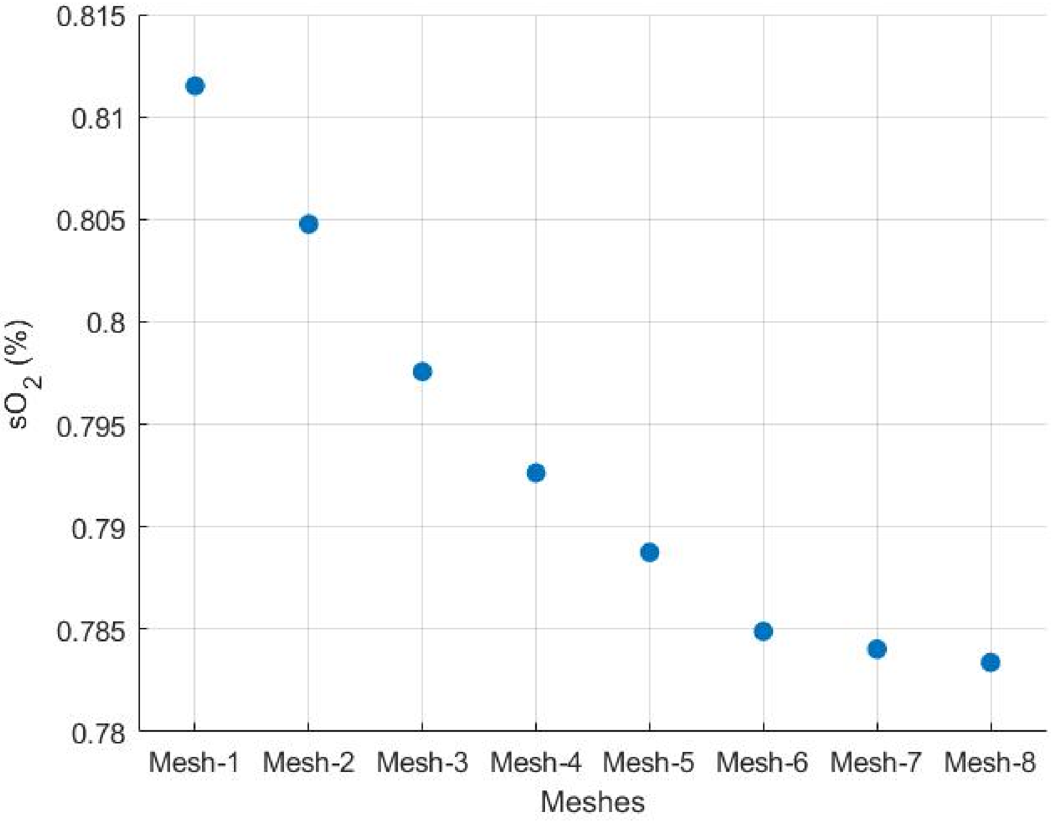

Figure 4.3. Mesh convergence of Carreau model for average oxygen saturation (sO_2) at the outlet for $Q_0 = 90\ ml/h$.

In the comparison of different meshes, Mesh-7 and Mesh-8 stand out due to their total element numbers and accuracy. The first six mesh structures are the same with the meshe used in Newtonian model mesh convergence study. Specifically, Mesh-7 has a total of 709,852 elements, while Mesh-8 contains a significantly higher total of 1,605,264 elements. Both meshes demonstrate commendable accuracy, with Mesh-7 and Mesh-8 showing percentile errors of 0.11% and 0.08%, respectively. These errors are obtained by comparing the average oxygen saturation values to the preceding mesh configurations. After careful consideration and analysis, Mesh-7 is selected for further studies, particularly for use in the Carreau model. This decision is based on a balance of element quantity, in other words computational cost, and the precision required for detailed analyses.

For further validation, comparisons with both numerical and experimental studies in the literature are conducted. Kaesler *et al.* [12] is chosen as the reference study to compare and validate the steady case results for the AR=40/3 geometry with the same boundary conditions. The study also contains other sources of both numerical and analytical studies having results for the same geometry and boundary conditions. The results obtained in this stdy is compared to all studies given in Kaesler *et al.* [12].

In Figure 4.4, the total oxygen transfer rate from oxygenator is compared for different volumetric flow rates. The reference study contains both numerical and experimental results. In addition to that, the results are also compared with analytical studies in the literature, such as the effective diffusivity model [8] and mass transfer correlation [21].

Both Newtonian and Carreau Models show acceptable agreement with mentioned studies in Kaesler *et al.* [12]. According to the results obtained, both models are within 30, 15, and 10 percent margin of errors for 20, 50, and 90 mL/h volumetric blood flows, respectively.

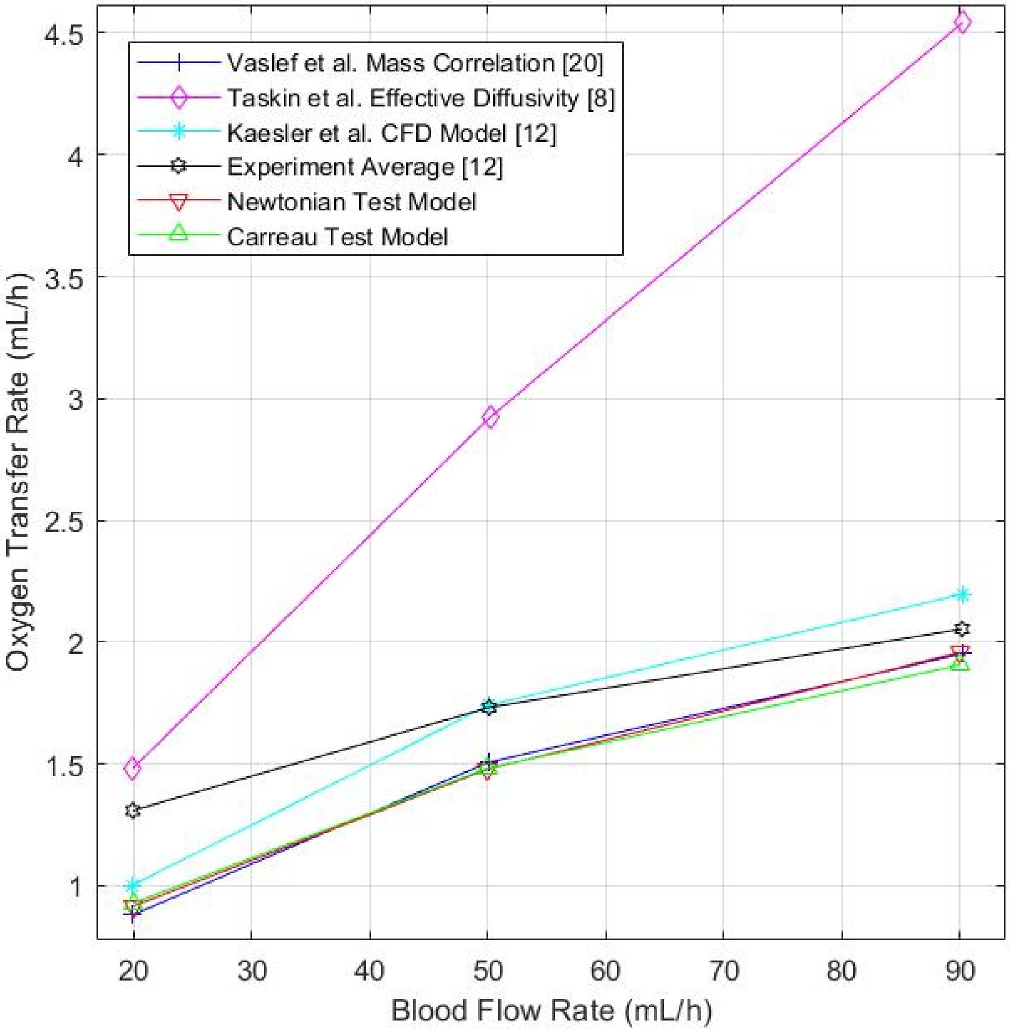

Figure 4.4. Comparing oxygen transfer rates for validation.

It should be underlined that, as expected, the Carreau Model shows results closer to experimental studies at low blood flow rate values. As the blood flow rate increases and thus the shear rate increases, the Newtonian Model starts to give more consistent values with experimental studies.

Oxygen transfer rates and their relative errors with respect to the average of the 3 experiments conducted in Kaesler's study [12] are given in Table 4.3.

Table 4.3. Oxygen transfer rates in mL/h and relative errors.

	20 mL/h		**50 mL/h**		**90 mL/h**	
	O_2 Transfer Rate (mL/h)	**Rel. Error**	**O_2 Transfer Rate (mL/h)**	**Rel. Error**	**O_2 Transfer Rate (mL/h)**	**Rel. Error**
Vaslef *et al.* Mass Correlation [21]	0.8804	32.74%	1.5073	12.96%	1.9519	4.97%
Taskin *et al.* Effective Diffusivity [8]	1.4825	13.25%	2.9257	68.94%	4.5438	121.22%
Kaessler *et al.* CFD [12]	1.0029	23.39%	1.7420	0.59%	2.1968	6.96%
Experiment-1 [12]	1.5233	16.37%	1.7318	0%	2.0335	0.99%
Experiment-2 [12]	1.2274	6.24%	1.6501	4.71%	2.0744	0.99%
Experiment-3 [12]	1.1866	9.35%	1.8032	4.12%	2.0233	1.49%
Experiment Average [12]	1.3090	-	1.7318	-	2.0540	-
Newtonian Test Model	0.9170	29.95%	1.4789	14.60%	1.9168	6.67%
Carreau Test Model	0.9298	28.97%	1.4826	14.39%	1.9069	7.16%

4.2. Transient Analysis

Following the steady-state analyzes, time-dependent analyzes are performed for the same geometry in which the pulsatile flow characteristics are examined. Transient results are observed to reach a periodic state before the outputs are compared with analytical and correlative studies. The pulsatile nature of the flow is fully observed independently of the initial conditions.

The oxygen saturation at the outlet is chosen for demonstration due to the long-lasting aggregation of oxygen molecules in the main channel. As seen in Figure 4.5, the oxygen saturation at the outlet converges to a periodic state and has the same saturation values for the consecutive periods after 13th.

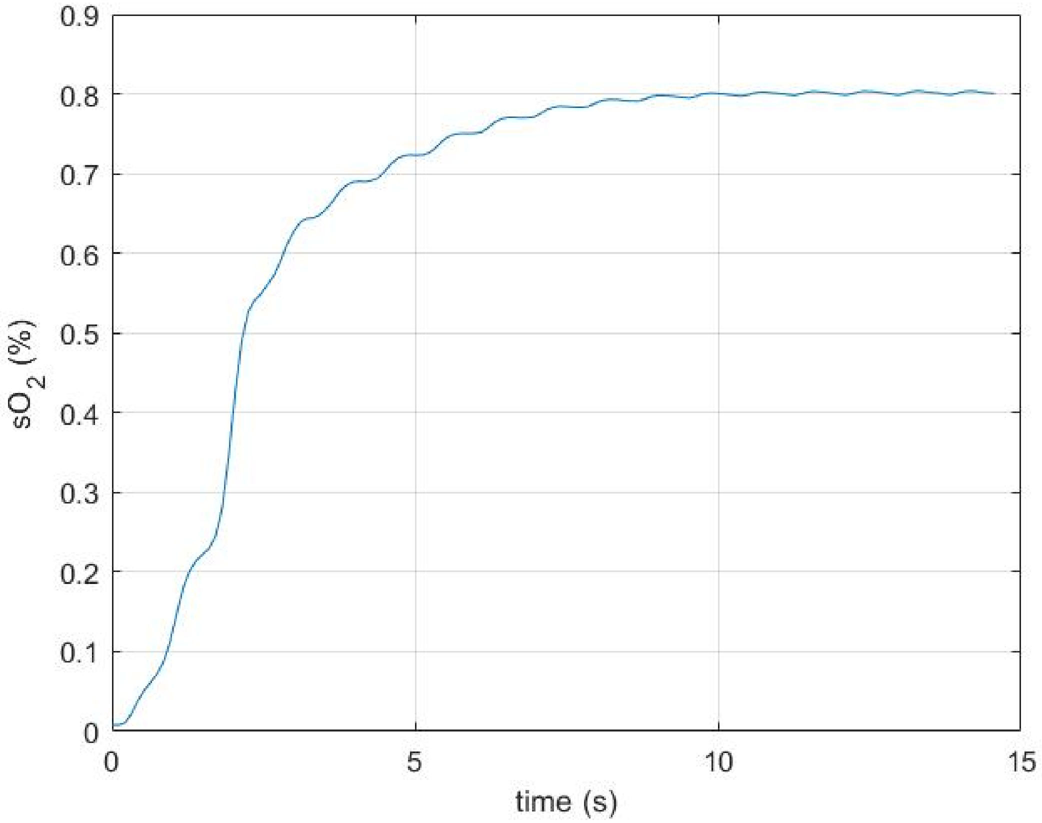

Figure 4.5. Average oxygen saturation in blood at the outlet for T=0-17.

For full validation of the model, comparisons are made with studies in the literature on dimensionless parameters such as the normalized drag and Sherwood number. Keller [22] defined the normalized drag per unit length $\bar{F}_D$ on each cylinder using the theory of lubrication, which is proved to be valid for concentrated arrays. It is expressed as

$$\bar{F}_D = \frac{F_D}{\mu U} = \frac{12\beta}{\left(1-\beta^2\right)^2} + \frac{18\beta}{\left(1-\beta^2\right)^{\frac{5}{2}}}\left(\arctan\left(\frac{\beta}{\sqrt{1-\beta^2}}\right) + \frac{\pi}{2}\right), \tag{4.1}$$

where F_D is the drag force and β is the blockage ratio being the ratio of cylinder radius to half of the vertical spacing between cylinders.

The normalized drag is found to be 32.7404 using Keller's correlation for the blockage ratio of the test geometry in this test study. The present time-averaged normalized drag values agree well with the above correlation with a mean of 33.4277 and standard deviation of 0.1266.

Sherwood number (Sh) is used to verify the transport analysis part of the model as it is frequently reported as a dimensionless parameter in other works. It represents the ratio of the convective mass transfer to the rate of diffusive mass transport and expressed as

$$Sh = \frac{h}{D_{c/L}} = \frac{\text{convective mass transfer rate}}{\text{diffusion rate}}, \tag{4.2}$$

where h represents the convective mass transfer coefficient, D_c denotes the mass diffusivity, and L is the characteristic length which is the membrane diameter D in this case.

In order to calculate the Sherwood number numerically, it is necessary to link the molar flux transferred at the fiber-blood interface to the difference between the concentrations at the interface $c_{\text{interface}}$ and the blood inlet c_{inlet} . This can be done by calculating the convective mass transfer coefficient over the domain. It can be expressed as

$$h_{\text{numerical}} = \frac{\int j ds}{(c_{\text{inter face}} - c_{\text{inlet}}) \times A_{\text{interface}}}, \tag{4.3}$$

where j denotes the molar flux at the interface and $A_{interface}$ refers to interface area. The calculated mass transfer coefficient is replaced into the Equation 4.3 and the global Sherwood number is numerically obtained.

In the literature, the Sherwood number relations are generated experimentally as a function of Reynolds numbers and Schmidt numbers for different geometries and flow types such as flow over a flat plate or flow over an array of cylinders. Schmidt number Sc is defined as the ratio of momentum diffusivity to mass diffusivity. It is referred to characterize fluid flows where momentum and mass diffusive convection processes occur simultaneously [23]. Schmidt number is expressed as

$$Sc = \frac{\nu}{D_c} = \frac{\mu}{\rho D_c} = \frac{\text{viscous diffusion rate}}{\text{molecular diffusion rate}}, \tag{4.4}$$

where ν is the kinematic viscosity.

The Churchill and Bernstein correlation [24], derived from experiments, is chosen for comparison with the numerical estimation obtained in this part. This correlation is widely used to estimate the mass transport over an array of cylinders. Considering the Reynolds and Schmidt numbers for the test case (Re=0.456, Sc=10543) and the flow type, this correlation is the best match for our geometry and conditions. The correlation is given as

$$Sh_{cor} = 0.3 + \left[0.62 (Re)^{\frac{1}{2}} (Sc)^{\frac{1}{3}} \times \left[1 + \left(\frac{0.4}{Sc} \right)^{\frac{2}{3}} \right]^{\frac{-1}{4}} \right] \times \left[1 + \left(\frac{Re}{282000} \right)^{\frac{5}{8}} \right]^{\frac{4}{5}}. \tag{4.5}$$

The results for both Sherwood numbers, numerically computed in this study and calculated using the Equation 4.5, are compared for the time-average of 17^{th} period in Figure 4.6. They agree well with mean absolute percentile error of 10.67%.

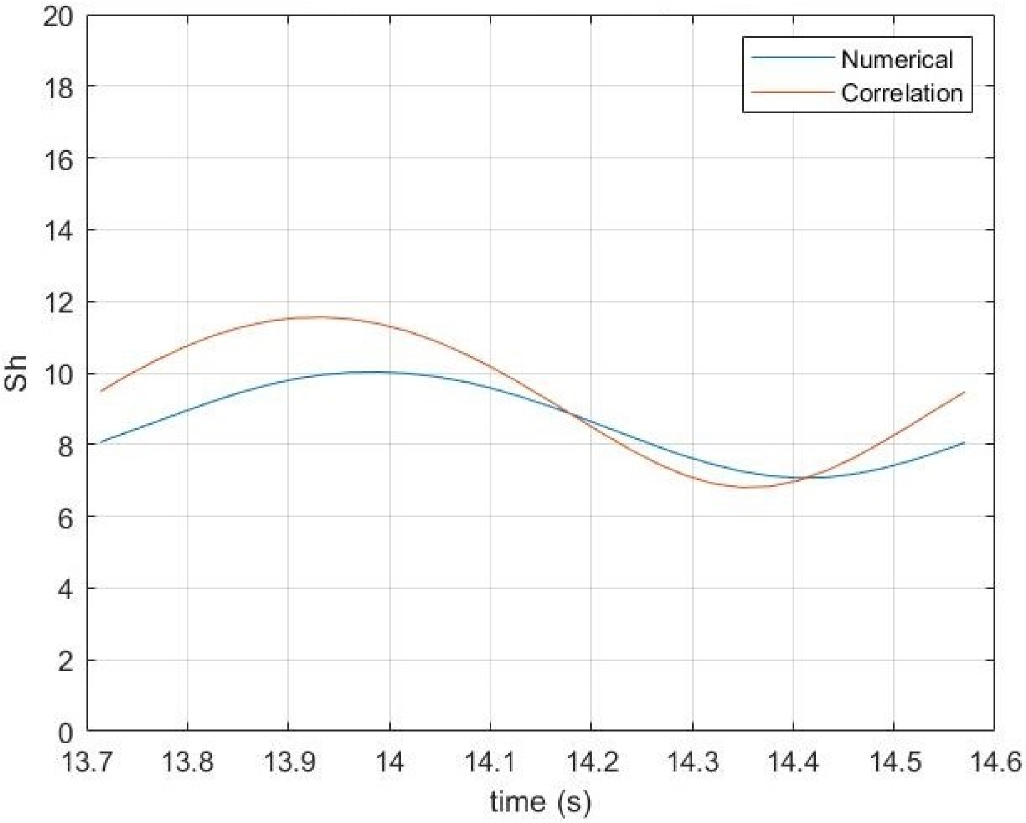

Figure 4.6. Sherwood number comparison of the correlation and the numerical results.

It is observed there is a small phase difference in the comparison since the value calculated by the correlation uses the Reynolds number with the velocity scale based on the sinusoidal flow rate function defined at the inlet, whereas the numerically calculated value is obtained directly from the gas transfer across the domain, causing a small delay in the response.

5. RESULTS AND DISCUSSION

5.1. Newtonian Case

Following tests and validation, four geometries with different aspect ratios (column-to-row ratios) —AR=60/2, AR=40/3, AR=20/6, and AR=10/12— are developed. The new configurations are deduced as aspect ratio variations of the reference geometry (AR=40/3) that is based on the average geometry characteristics of real products. These four geometries correspond to array configurations of 2×60, 3×40, 6×20, 12×10 ($rows\times columns$) respectively. This allows examining the impact of the aspect ratio on the flow, pressure drop, mass transfer, shear stress characteristics, and biocompatibility measures.

For all of the four geometries, both the distance between the membranes and the membranes-to-walls distances are preserved. Also, the entry and exit lengths before and after the fiber bundle are kept constant. In this way, the change in aspect ratio only result in scaling of the bundle.

5.1.1. Flow Results

The velocity contours are displayed to observe high speed areas and stagnant regions in Figure 5.1 for $\omega t = 0.5\pi$ where the inlet pulsation is at its maximum. The fiber bundles in the figures are selected as the middle ones in both vertical and horizontal directions for all configurations to compare the same region with each other. As a result, areas of high flow speeds are observed in the narrow regions between the membranes and where the membranes approach the walls. In addition, stagnant regions, which are areas of low flow speeds, develop in the wake of fiber bundles.

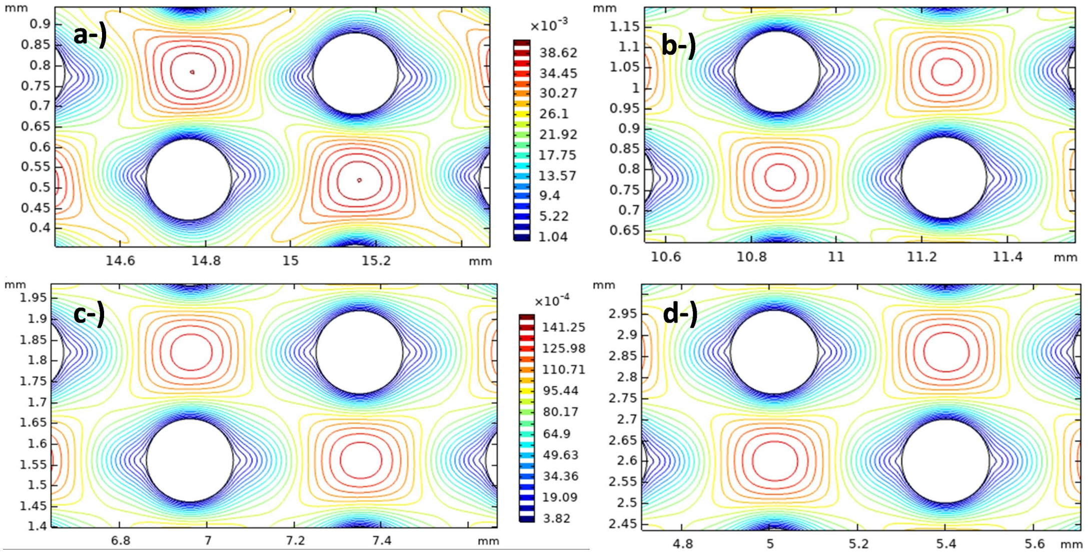

Figure 5.1. Velocity contours for (a) AR=60/2, (b) AR=40/3, (c) AR=20/6, and (d) AR=10/12 at peak pulsation in m/s.

Velocity contours show that the boundary layers get thicker as the number of rows decrease and the number of columns increase. With the exception of the AR=60/2 configuration, which is altered by the wall effect, the velocity fields around the fibers maintain their symmetry features. The stagnant regions are observed to move up for the bottom fibers and to move down for the top fibers.

As expected, no recirculation zone exists even in peak pulsation magnitude due to the low Reynolds number as shown in streamlines given in Figure 5.2. Denser streamlines show that configurations with high aspect ratio have higher velocity gradients around the membrane leading to an increase in convection and resulting in a better gas transfer. Although the stagnant region in the wake lowers the gas transfer efficiency as the gas transfer mechanism is then driven mostly by diffusivity and a negligible share of convection, the efficiency is better when compared to the cases with recirculation region. This is due to the fact that the fluid is semi-trapped in recirculation regions leading to lower concentration gradients [5].

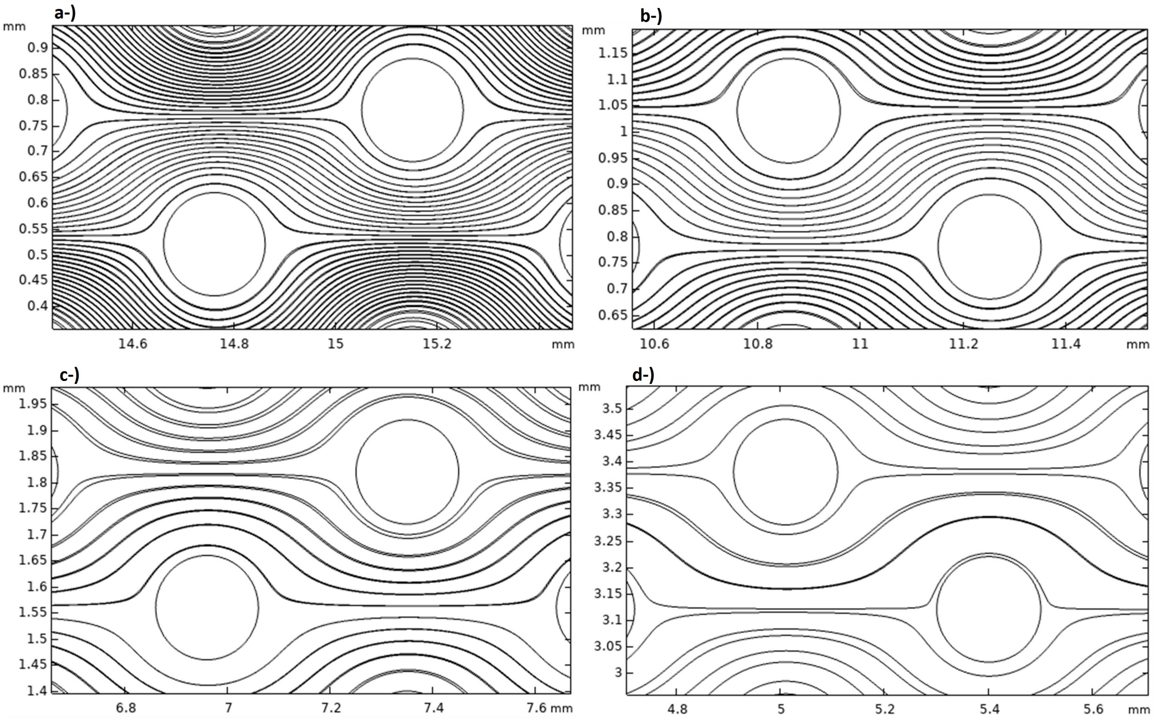

Figure 5.2. Flow streamlines at peak pulsation for (a) AR=60/2, (b) AR=40/3, (c) AR=20/6, and (d) AR=10/12.

5.1.2. Pressure Drop Results

Pressure drops across the domains and time averaged normalized drags on one membrane are obtained by using Equation 4.1. Both parameters are shown in Table 5.1. Pressure drops are given at the peak pulsation instances where highest values are observed. Pressure drop is obtained by the difference of average blood pressure at the inlet and the outlet.

The pressure drops increase with increasing aspect ratio. This is caused by the larger velocity magnitudes imposing higher drag on the membranes. Despite the differences in magnitude, the ratios of peak to bottom pressure drops are conserved for all geometries.

Table 5.1. Pressure drop at peak pulsation and normalized drag for all configurations.

	2 × 60	**3 × 40**	**6 × 20**	**12 × 10**
Pressure Drop at Peak Pulsation (Pa)	220.18	100.62	26.38	7.26
Time-Averaged Normalized Drag on One Membrane	35.02	33.55	31.93	30.90

In Table 5.2, the steady-state results are also given for each configuration. Both pressure drop and average normalized drag values are similar for steady flow and the means of pulsatile flow.

Table 5.2. Pressure drop and normalized drag comparison of all configurations in steady-state.

	2 × 60	**3 × 40**	**6 × 20**	**12 × 10**
Pressure Drop (Pa)	145.66	67.10	17.35	4.39
Normalized Drag on One Membrane	34.90	33.43	31.82	30.79

5.1.3. Gas Transfer Results

The oxygen partial pressure distributions surrounding the fibers and, consequently, the concentration boundary layers at the fiber-blood interface, determine the gas transport properties [25].

The undermost fiber in the fourth column is selected for each configuration for local analysis. The reason for this is to be able to examine a fiber that is relatively far from the inlet and where the wall effect can be examined locally.

In Figure 5.3, the local flux magnitude around the same fiber for different configurations is displayed with respect to angular position around the fiber. This angular position ϕ is measured starting from the stagnation point on the rear side. That means $\phi = 180$ corresponds to the lead point of the cylinder.

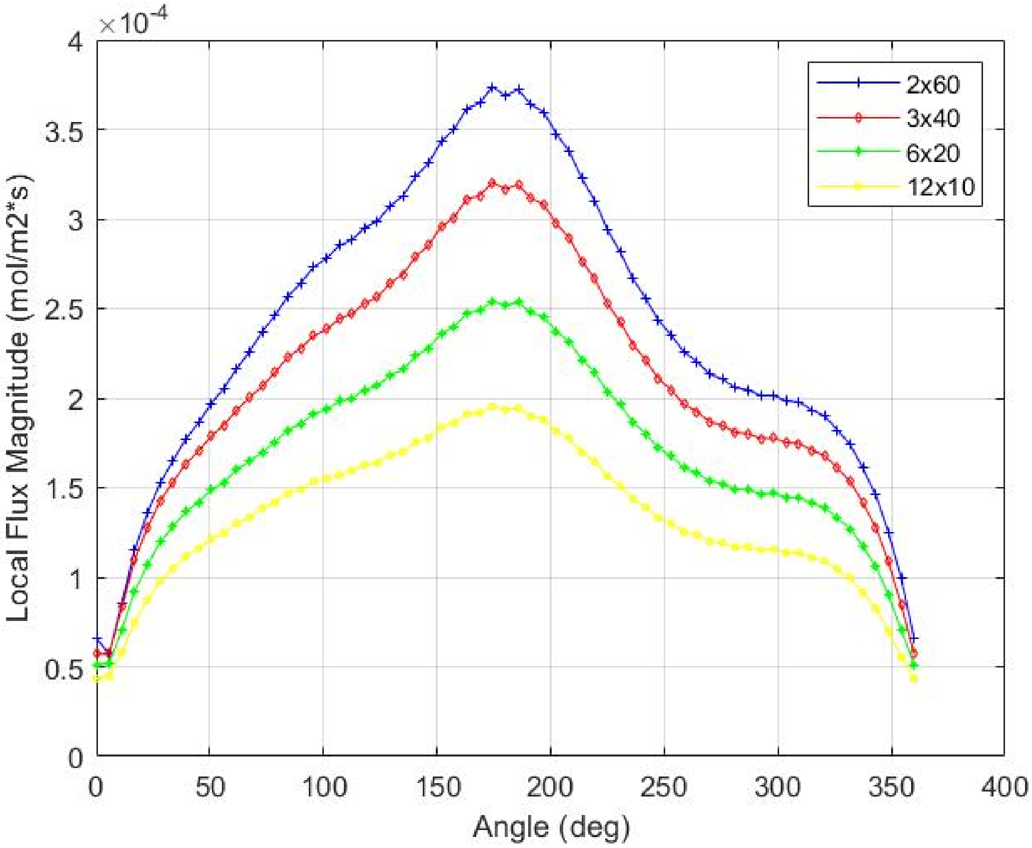

Figure 5.3. Local flux magnitude around the chosen membrane for all configurations.

The local flux magnitude, which is an indicator of the gas transfer at fiber-blood interface, is heavily influenced by the velocity field. When the velocity gradient is high, it leads to high partial pressure gradient and gas transfer. For different configurations, the wake regions are observed to perform equally whereas the gas transfer at the top and bottom parts of the fibers differ significantly.

It is also noteworthy that fluxes tend to decrease at 180° due to the resulting small stagnant region around the leading edge of the fibers where a maximum is expected but a local minimum is observed. This distinction is particularly noticeable for AR=60/2 and AR=40/3 configurations since velocity gradients around the stagnant region are higher for increasing aspect ratio.

It is also remarkable that the gas transfer performance is lower for 180° $< \phi <$ 360° than 0° $< \phi <$ 180° and this is due to the wall effect on the fibers at the bottom of the main channel. The diffusion towards the bottom is limited by the wall. As a result, oxygen molecules are aggregated near the membrane on the wall side and this causes concentration boundary layer on the wall side getting thicker. The reverse is also valid for the fibers at the top. Oxygen gas transfer for the fibers at the top of the main channel is lower for 0° $< \phi <$ 180° which corresponds to the wall side.

When the concentration distribution is examined, Figure 5.4 demonstrates that as the aspect ratio drops, the aggregation surrounding the fiber becomes denser due to the thickening of the partial pressure boundary layer of oxygen around the fiber. Lower partial pressure gradients around the fiber are caused by thicker velocity boundary layers, which also lead to lower mass transfer coefficients and less effective gas transport at the fiber surface.

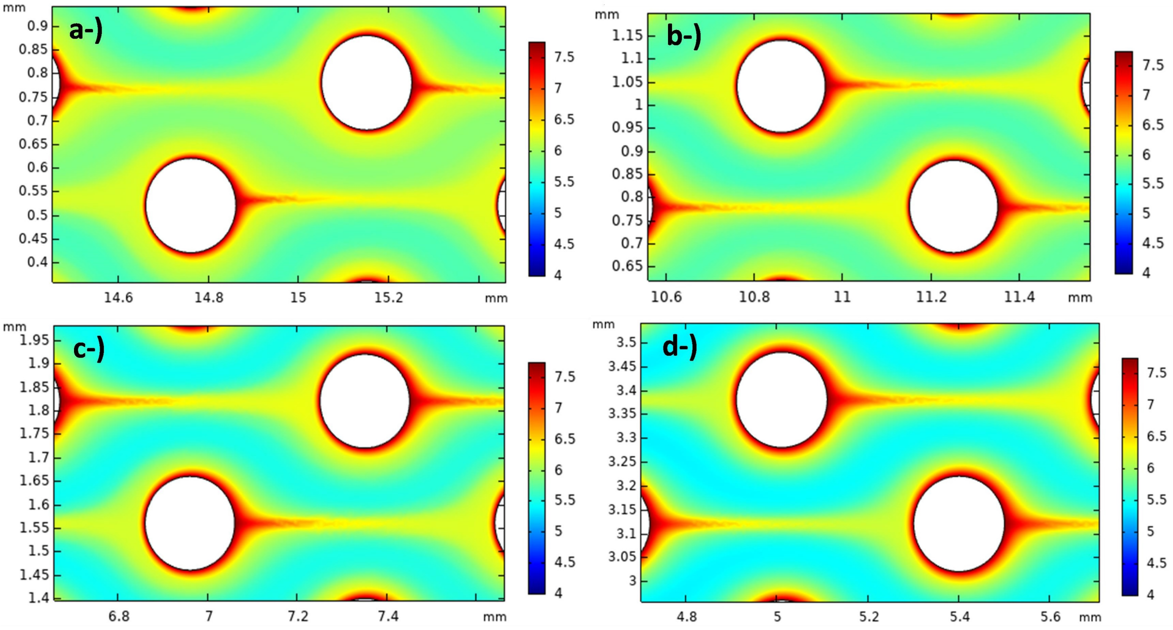

Figure 5.4. Concentration distribution at peak pulsation for (a) AR=60/2, (b) AR=40/3, (c) AR=20/6, and (d) AR=10/12.

The overall gas transport performances are examined and compared for different geometries using the oxygen transfer rates at the membranes and time-averaged oxygen saturation rates at the outlet. The outlet oxygen saturation decreases as the aspect ratio drops, as shown in Table 5.3.

Table 5.3. Time-averaged oxygen saturation level at the outlet for the last period.

	2 × 60	**3 × 40**	**6 × 20**	**12 × 10**
Oxygen Saturation (%)	80.30	79.11	77.05	73.38

The oxygen transfer rate values are given in Figure 5.5 and show also similar trends compared to the saturation values.

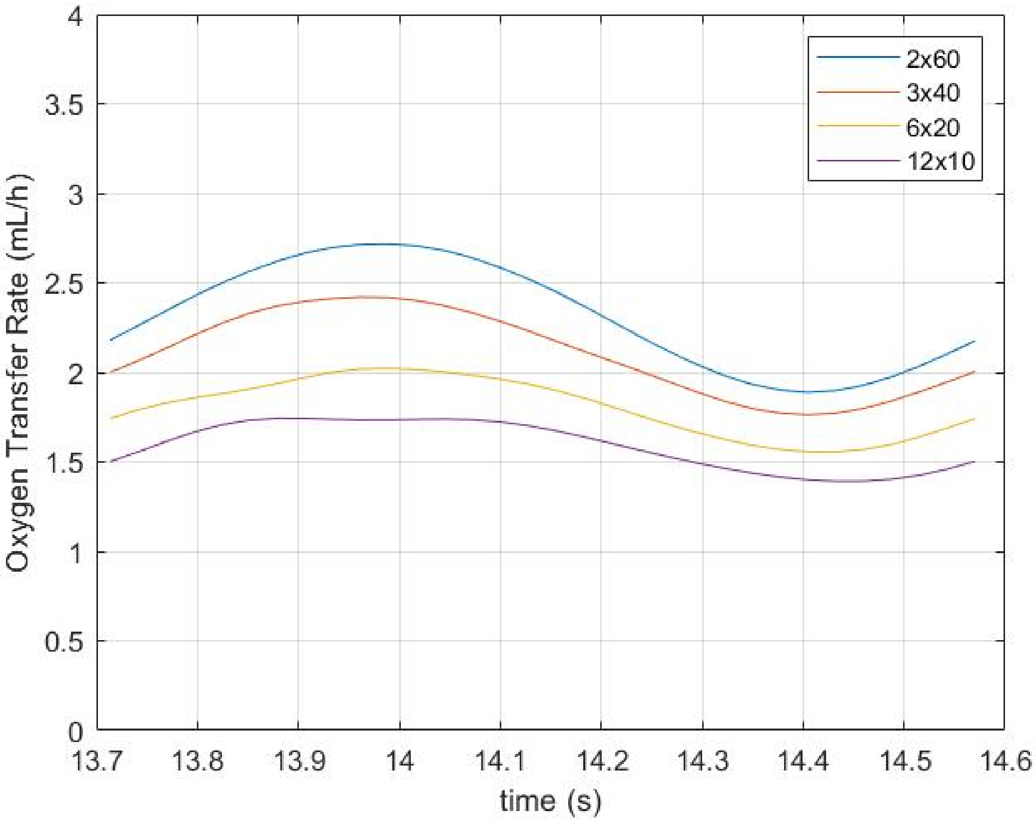

Figure 5.5. Oxygen transfer rates for the last period.

Since the overall oxygen transfer rates for the AR=60/2 and AR=40/3 configurations are similar, it makes sense to take the shear stress and pressure drop values into account in addition to the gas transfer characteristics when deciding which configuration to choose.

Results for the total oxygen transfer rate at the membranes and the outlet oxygen saturation are shown in Table 5.4 for steady state cases. It is notable that the mean oxygen transfer rates for pulsatile flow for the AR=20/6 and AR=10/12 configurations exhibit similar results with steady flow gas transfer characteristics. When taking into account the mean value over a period, the pulsatile flow appears to be performing higher oxygen transfer rates for the AR=60/2 and AR=40/3 geometries.

Table 5.4. Saturation and oxygen transfer rate comparison of all configurations in steady-state.

	2×60	**3×40**	**6×20**	**12×10**
Oxygen Saturation (%)	78.33	78.11	77.92	77.12
Oxygen Transfer Rate (mL/h)	1.9921	1.9168	1.8225	1.6042

5.1.4. Shear Stress Results

To ensure biocompatibility, the shear stress is crucial. Since the transient analysis mimics the variations in shear stress, it can be seen whether the maximum and minimum values are outside of what is considered to be permissible bounds.

In Figure 5.6, the maximum shear stresses are displayed throughout the domain at peak pulsation and the same region is recorded to have the maximum value for all configurations which is the bottom part of the bottom fiber in the second-to-last column for all configurations. The highest WSSs at the peak of the pulsation are recorded as 2.8380 Pa for the AR=60/2 configuration, 1.9467 Pa for the AR=40/3 configuration, 0.9972 Pa for the AR=20/6 configuration, and 0.5034 Pa for the AR=10/12 configuration.

The highest permissible WSS limit was discovered to be 1.2 Pascal when the earlier research on EC cultured membranes were evaluated [26]. Studies published in the literature have suggested that this value should not be surpassed, despite the fact that it is also related to the duration of exposure to shear stress [27]. This is essential to prevent an undesirable increase in P-selectin levels, which are a symptom of EC inflammation. P-selectin platelets contribute to the buildup of the tissue factor that is known to cause thrombi to form [28].

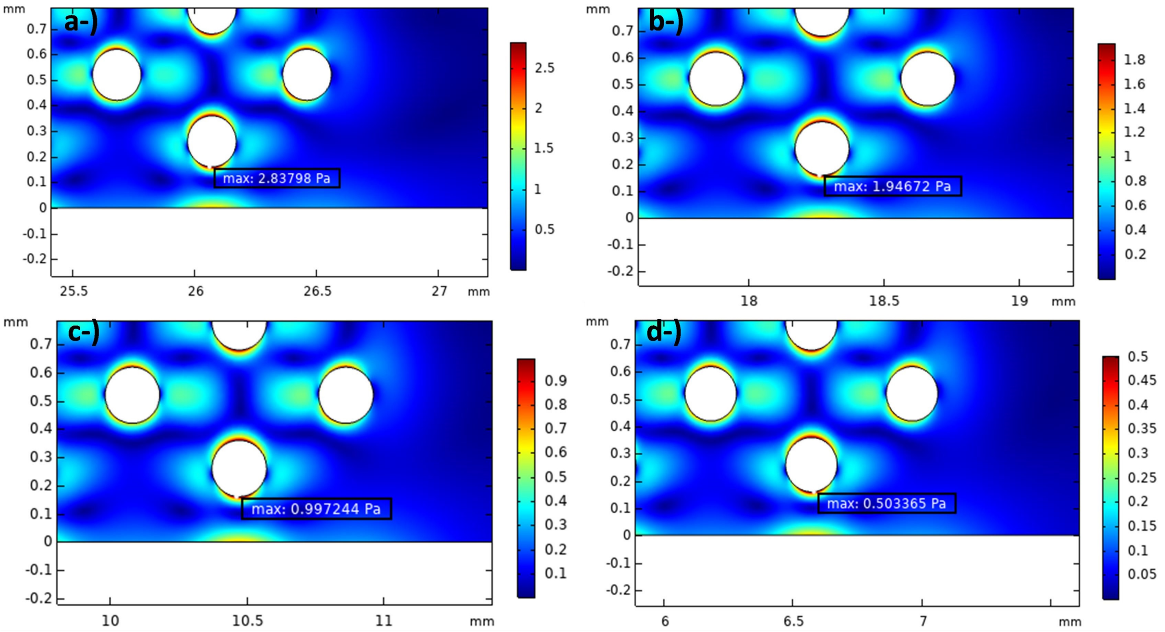

Figure 5.6. Shear stress distribution in Pa around maximum value in the domain at peak pulsation.

Thrombi or blood clots are very dangerous since they may lead to a lethal condition called pulmonary embolism, when a clot blocks a lung artery. This makes it difficult for the heart to pump blood to the lungs, causing heart failure. This blockage may also prevent oxygen from getting into the bloodstream, leading to severe problems like shock and organ failure. Therefore, when designing a microfluidic artificial lung, it is necessary to consider a design based on wall shear stress values that will not trigger the blood coagulation mechanism.

Figure 5.7 depicts the time-dependent variations in maximum shear stresses for different geometries. The highest WSS values exhibit a growth of more than twofold during the period. The maximum WSS levels, even for the AR=60/2 configuration which has the highest values, are tolerable at the lowest pulsation.

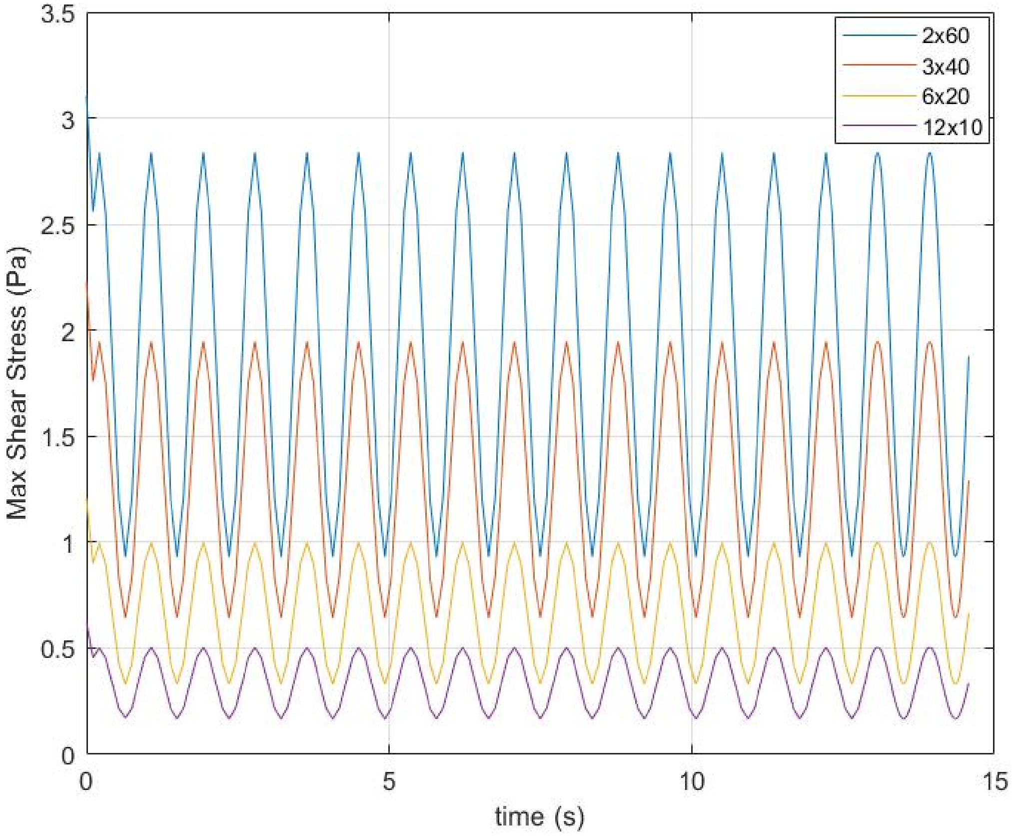

Figure 5.7. Maximum WSS for each configuration.

Maximum and minimum WSS values are given for steady-state analysis in Table 5.5. Maximum WSS values of steady flow are similar to that of the time-average of pulsatile flow.

Table 5.5. Maximum and minimum WSS comparison for all configurations in steady-state.

	2×60	**3×40**	**6×20**	**12×10**
Max WSS (Pa)	1.8755	1.2910	0.6742	0.3356
Min WSS (Pa)	0.0143	0.0105	0.0024	0.0024

5.1.5. Newtonian Results Evaluation and Discussion

When the results of four different geometries are examined, it is seen that only the AR=20/6 and AR=10/12 geometries are within the biocompatible limits, while the AR=40/3 configuration is slightly outside the limits. The fact that the oxygen transfer performances of AR=60/2 and AR=40/3 results are significantly higher than the other two configurations, but close to each other, shows that the oxygen transfer performance converges with increasing aspect ratio.

First reason for gas transfer performance to converge is that as the number of columns increases, rising oxygen saturation in blood along the channel reduces oxygen partial pressure gradients. This decelerates an effective oxygen transfer. In Figure 5.8, the average saturations of the section lines drawn from the middle of the membrane columns are shown. As the number of columns increases, as observed from the slope of the curve, the rate of increase in saturation decreases towards the end of the channel.

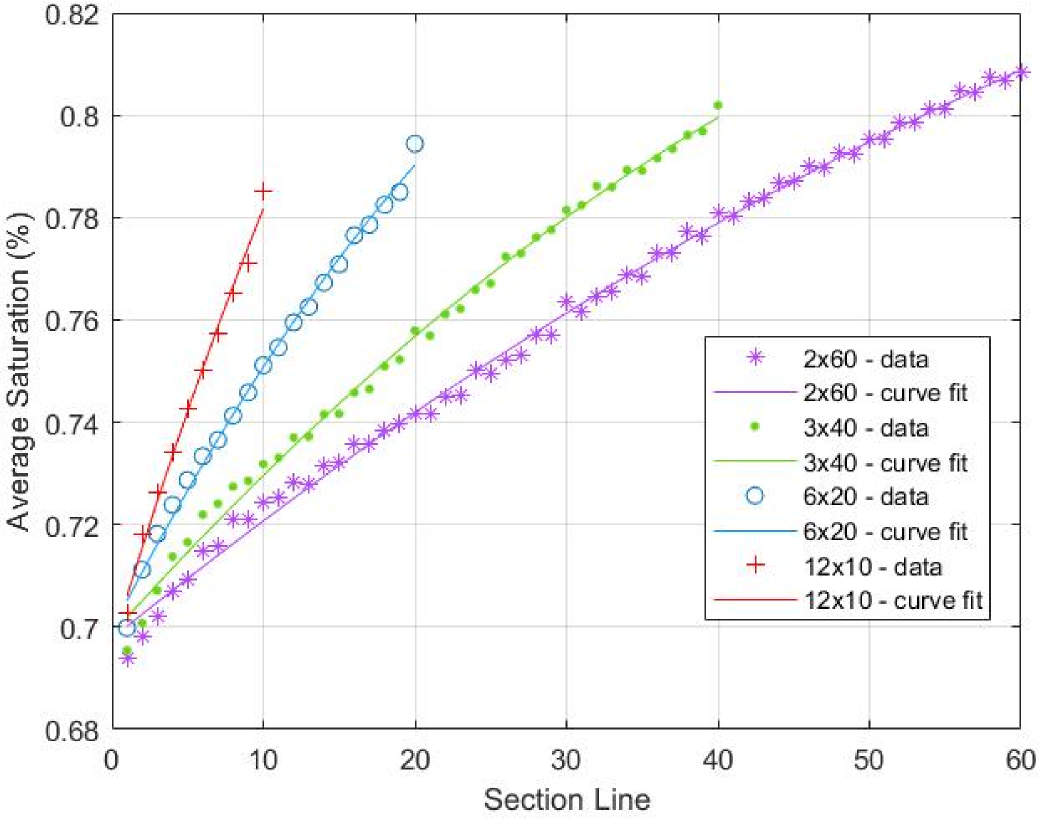

Figure 5.8. Average saturation in the section lines between columns.

Another reason is that although the speed increase in high aspect ratios due to constant volumetric flow has a positive effect on gas transfer performance, the large number of rows increases the efficiency, particularly in the first columns. In Figure 5.19, the total gas transfer of the columns for each configuration is given separately.

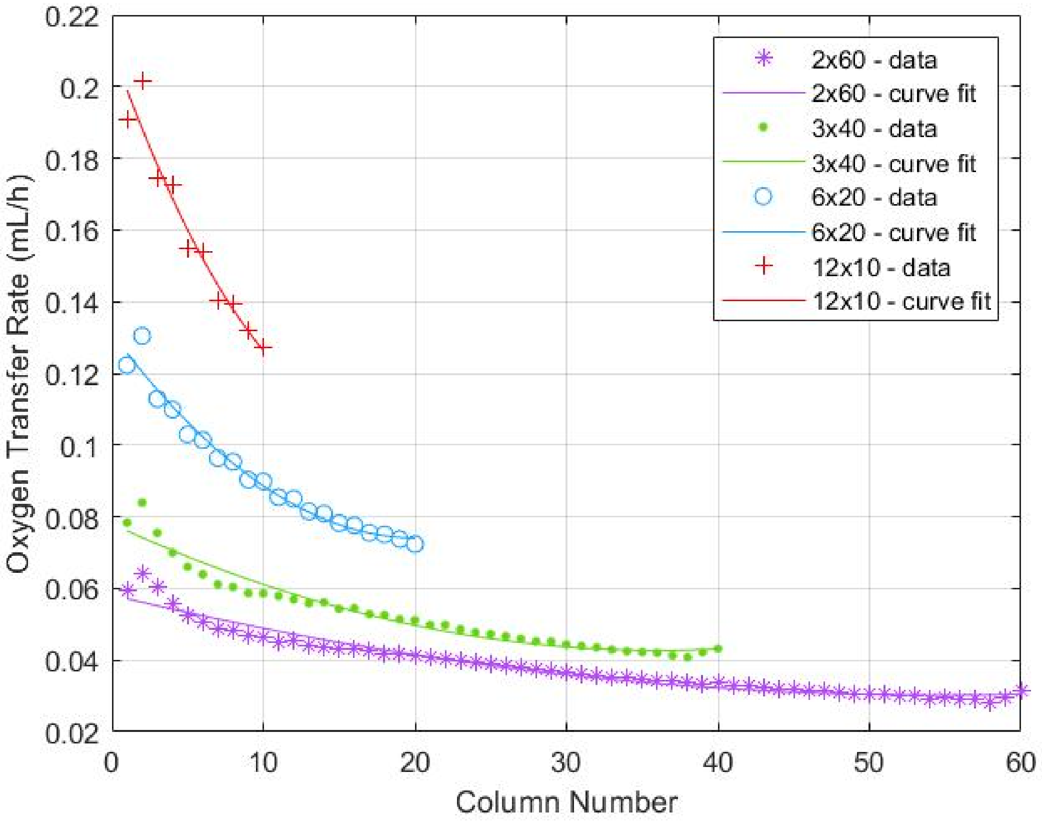

Figure 5.9. Total oxygen transfer rate of columns for each configuration.

As a result of these, it has been suggested that geometries with AR=30/4 and AR=24/5 could be tested to obtain a configuration that is both biocompatible and has high gas transfer performance. The time-averaged outlet saturation vs. aspect ratio is given with added configurations in Figure 5.10 for comparison and showing the convergence. As expected, new configurations perform better gas transfer rates than biocompatible configurations, namely AR=20/6 and AR=10/12. The fact that the AR=24/5 and AR=30/4 perform well compared to the AR=20/6 and AR=40/3 in terms of oxygen transfer performance is promising for these configurations. They have the potential to be an intermediate option that is both similar in oxygen transfer performance to the AR=40/3 configuration, which is just outside the biocompatible limits, and also is within acceptable biocompatible limits like the AR=20/6 configuration.

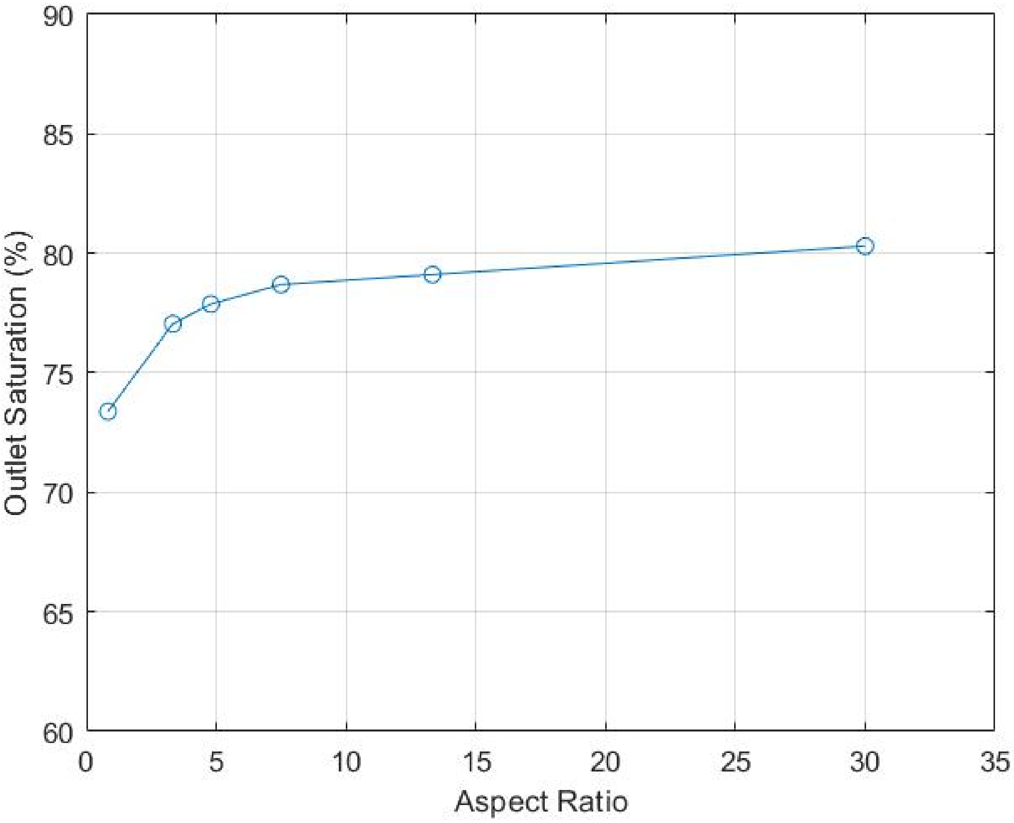

Figure 5.10. Time-averaged outlet saturation vs. aspect ratio.

The maximum WSS values are investigated to evaluate the biocompatibility. The maximum WSS values oscillates between 0.6425 Pa and 1.9481 Pa with 1.2930 Pa on average for AR=40/3, between 0.4900 Pa and 1.4819 Pa with 0.9849 Pa on average for AR=30/4, between 0.3949 Pa and 1.1931 Pa with 0.7935 Pa on average for AR=24/5, and between 0.3304 Pa and 0.9979 Pa with 0.6639 Pa on average for AR=20/6.

According to the maximum WSS values obtained, AR=24/5 configuration remains within the limits of biocompatibility, while AR=30/4 configuration is outside the acceptable limits during the peak flow rate. This makes the AR=24/5 configuration the most optimal choice. The fact that the oxygen transfer performance converges to a plateau with the increase of the aspect ratio value and that the AR=24/5 configuration is at the exact boundary in terms of WSS limits confirms this. Pressure drops through the channel are given for the best alternatives in Newtonian Model in Table 5.10.

Table 5.6. Pressure drops for the best alternatives.

	3 × 40	**4 × 30**	**5 × 24**	**6 × 20**
Pressure Drop (Pa)	100.62	58.02	38.47	26.38

5.2. Non-Newtonian Case and Comparison with Newtonian Results

The configurations AR=3x40, AR=4x30, AR=5x24, and AR=6x20, which are thought to give the best results among the geometries evaluated with the Newtonian model, are re-evaluated by non-Newtonian modeling for the transient case. For this purpose, the Carreau model, which is frequently used in blood modeling, is preferred as described in Chapter 2. The analysis outputs evaluated in Newtonian modeling are given in the same way, and the results obtained are compared for the two models.

5.2.1. Flow Analysis

Velocity contours for peak pulsation are given in Figure 5.11 to show the velocity field for the Carreau model. High speed areas and stagnant regions are similar to the Newtonian model.

As can be seen from the contours, no circulation zones are observed in the wake regions of the membranes due to the low Reynolds number. The trend of the boundary layers to thicken as the number of rows increases is the same as the Newtonian case. There is less than one percent reduction on average when considering the velocity field.

When implementing the Carreau model, another important parameter shaped by the flow is the shear rate. Shear rate, which has no effect on viscosity in the Newtonian model, is the determinant of viscosity in the Carreau model. This directly affects the flow.

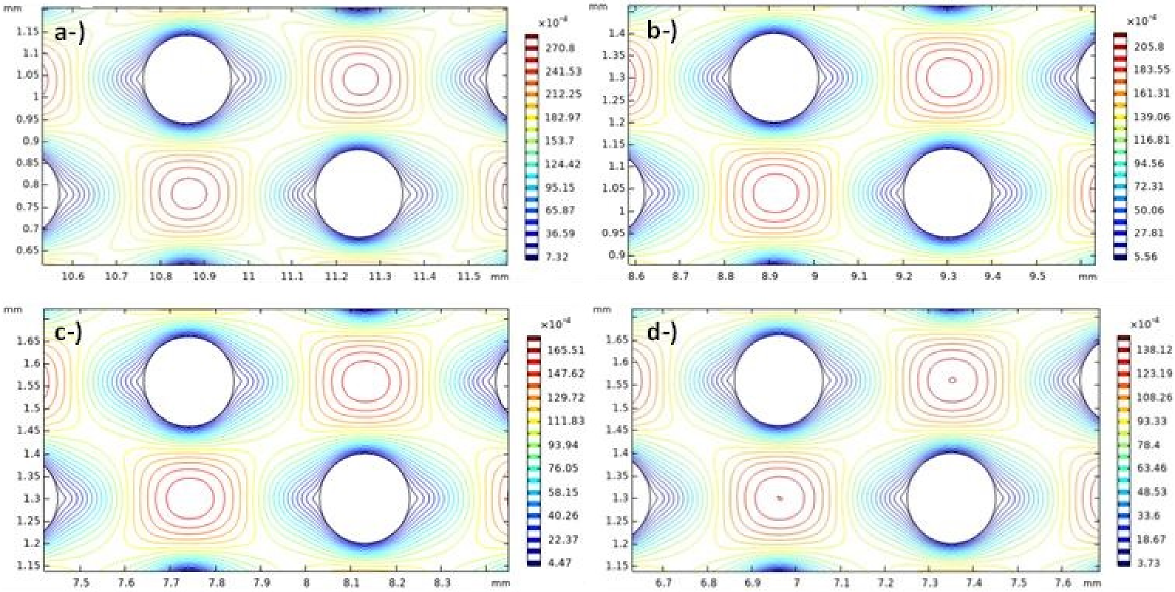

Figure 5.11. Velocity contours for (a) AR=40/3, (b) AR=30/4, (c) AR=24/5, and (d) AR=20/6 at peak pulsation in m/s.

In Figure 5.12, viscosity vs. shear rate is given for Carreau and Newtonian models [29].

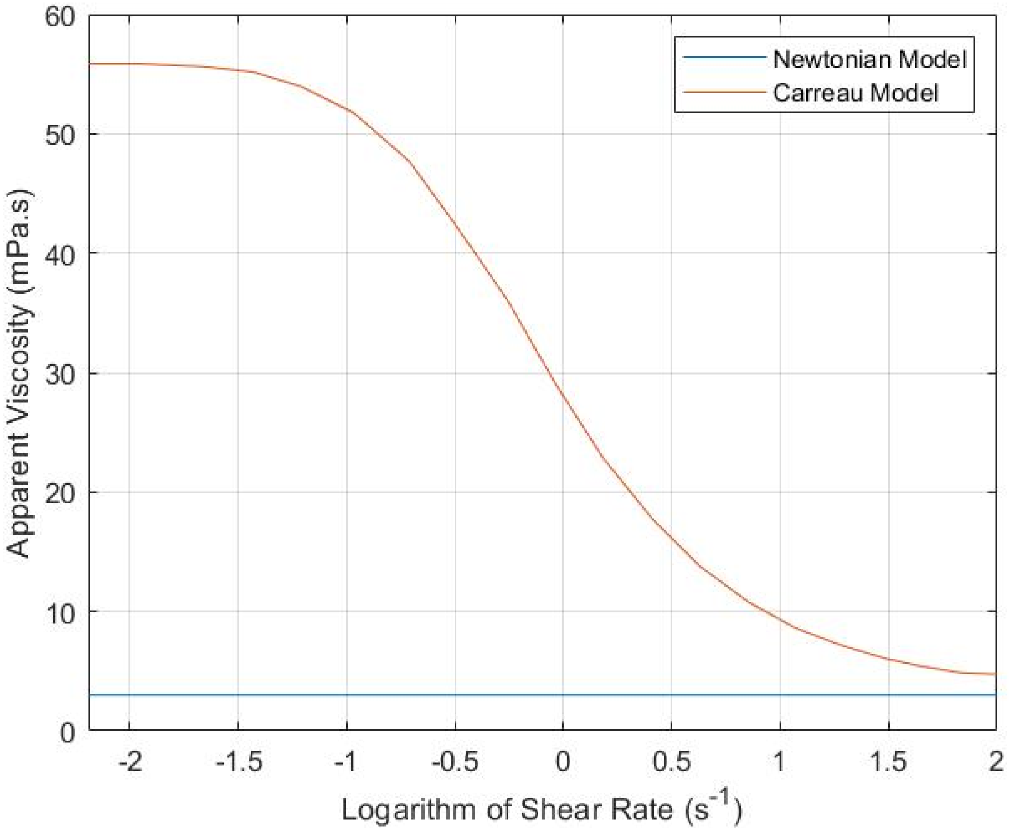

Figure 5.12. Shear rate vs. viscosity for Carreau and Newtonian model.

As can be seen from the viscosity vs. shear rate graph, while viscosity is fixed to a constant value for the Newtonian model, it changes very quickly between $10^{-1.5}$ s^{-1} and 10^{2} s^{-1} in the Carreau model. In a situation where the average shear rate oscillates between these values, it may not be possible for the Newtonian model to fully capture the viscosity-dependent flow properties. In order to see the effect of shear rate in viscosity, the average shear rates along the channel are given for the Carreau model in Figure 5.13 for each configuration.

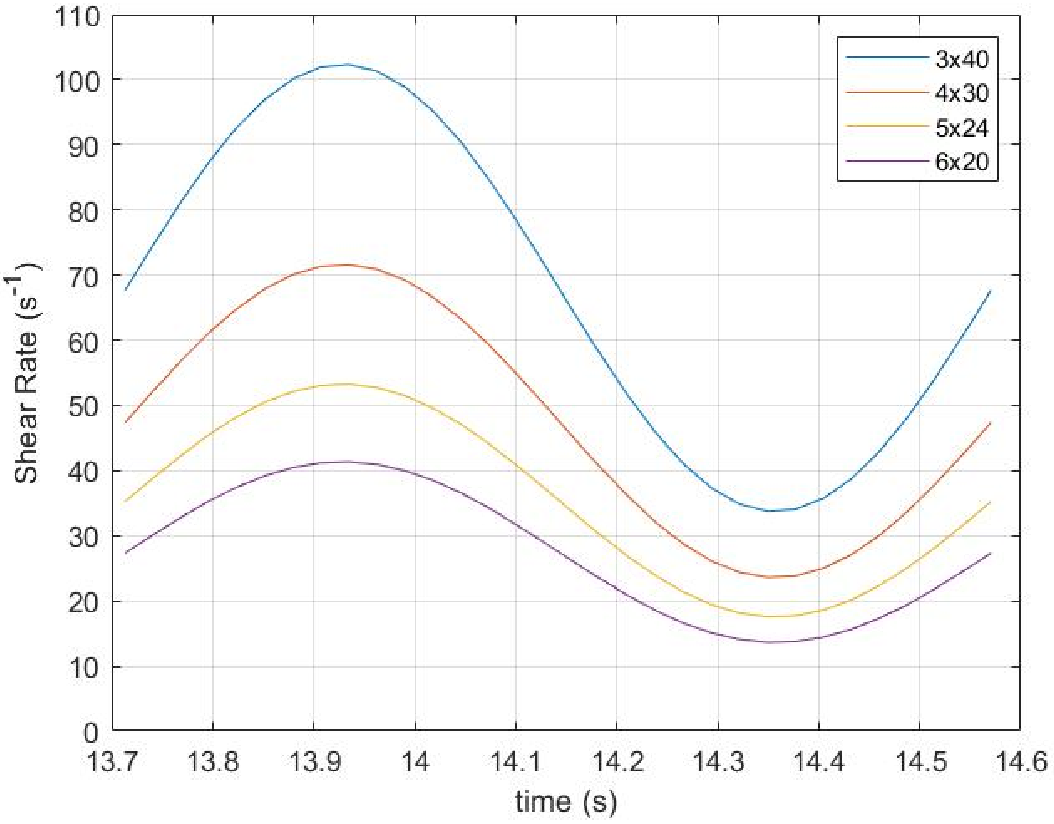

Figure 5.13. Average shear rates throughout the channel for different configurations.

It is clear that the average channel shear rate oscillates in the transition zone for the viscosity. This means the Carreau model is useful to capture consistent viscosity values for the blood flow in this problem.

5.2.2. Pressure Drop Analysis

Pressure drop values, which are important for a system where cardiac cycle will be sufficient without the need for an extra pump, are given in Table 5.7 for the Carreau model along with the time averaged normalized drag on one membrane.

Table 5.7. Pressure drop at peak pulsation and normalized drag for all configurations in Carreau model.

	3×40	**4×30**	**5×24**	**6×20**
Pressure Drop at Peak Pulsation (Pa)	144	84	57	41
Time-Averaged Normalized Drag on One Membrane	9176.5	9961.3	10621.2	10787.2

It should be noted that the pressure drop values increase with increasing aspect ratio as expected, however it is significantly higher compared to the Newtonian case. Nonetheless, the difference between configurations is narrowed in terms of ratio. The ratio of pressure drops between Newtonian and Carreau model is 1.43 for AR=40/3 and 1.58 for AR=20/6.

One of the most important changes in the results obtained with the Carreau model is the average normalized drag on one membrane. It is increased by more than 330 times approximately compared to the Newtonian model for all configurations. According to the Newtonian modeling results, it increases as the aspect ratio increases, while the opposite is true in the Carreau model. The reason for this is that the drag value increases more compared to the Newtonian model as the aspect ratio decreases. As the aspect ratio decreases, the shear rate decreases, and as a result, the difference between the drag values of the Newtonian and the Carreau models increases.

5.2.3. Gas Transfer Analysis

Oxygen transfer, which is one of the main parameters determining the performance of the microfluidic artificial lung, is re-examined with the results of the Carreau model. Oxygen transfer rates of four different configurations are given in Figure 5.14 for the last period.

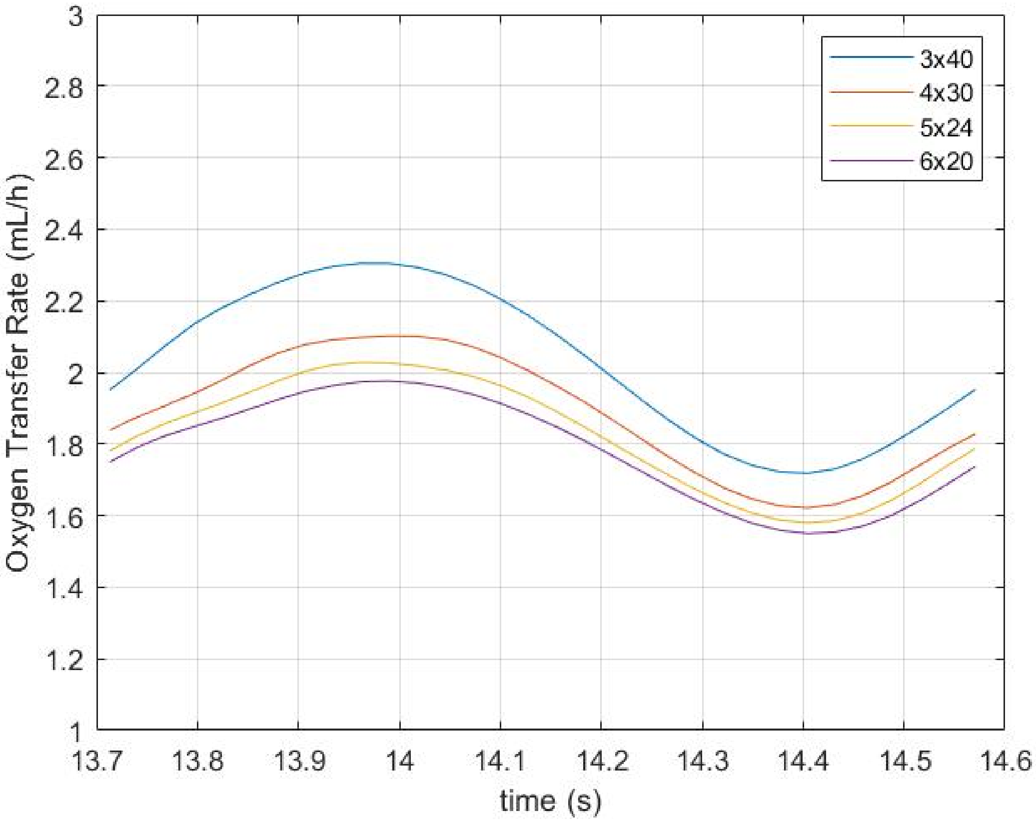

Figure 5.14. Oxygen transfer rates of the Carreau model for different configurations.

A decrease in oxygen transfer is seen compared to the results of the Newtonian model. Convergence of oxygen gas transfer that is observed in the Newtonian model is not observed in the Carreau model. As the aspect ratio increased, the oxygen gas transfer rate continued to increase. The time-averaged oxygen transfer rates for two models are given in Table 5.8 along with their percentile differences.

Table 5.8. Oxygen transfer rates for the Newtonian and the Carreau models.

	3 × 40	**4 × 30**	**5 × 24**	**6 × 20**
Oxygen Transfer Rate Newtonian Model (mL/h)	2.1023	2.0096	1.9010	1.8027
Oxygen Transfer Rate Carreau Model (mL/h)	2.0270	1.8826	1.8222	1.7809
Percentile Difference (%)	3.71	6.74	4.33	1.22

Oxygen transfer analysis is also done for the local performance around the same membrane with Newtonian model. The flux distribution shows similar trend with Newtonian model except for the peak point where the angle $\phi = 180°$ corresponds to the leading edge of the membrane. The flux tends to converge to a plateau rather than to a peak point as in Newtonian model. The local flux magnitude for the same membrane as in Newtonian results is given in Figure 5.15.

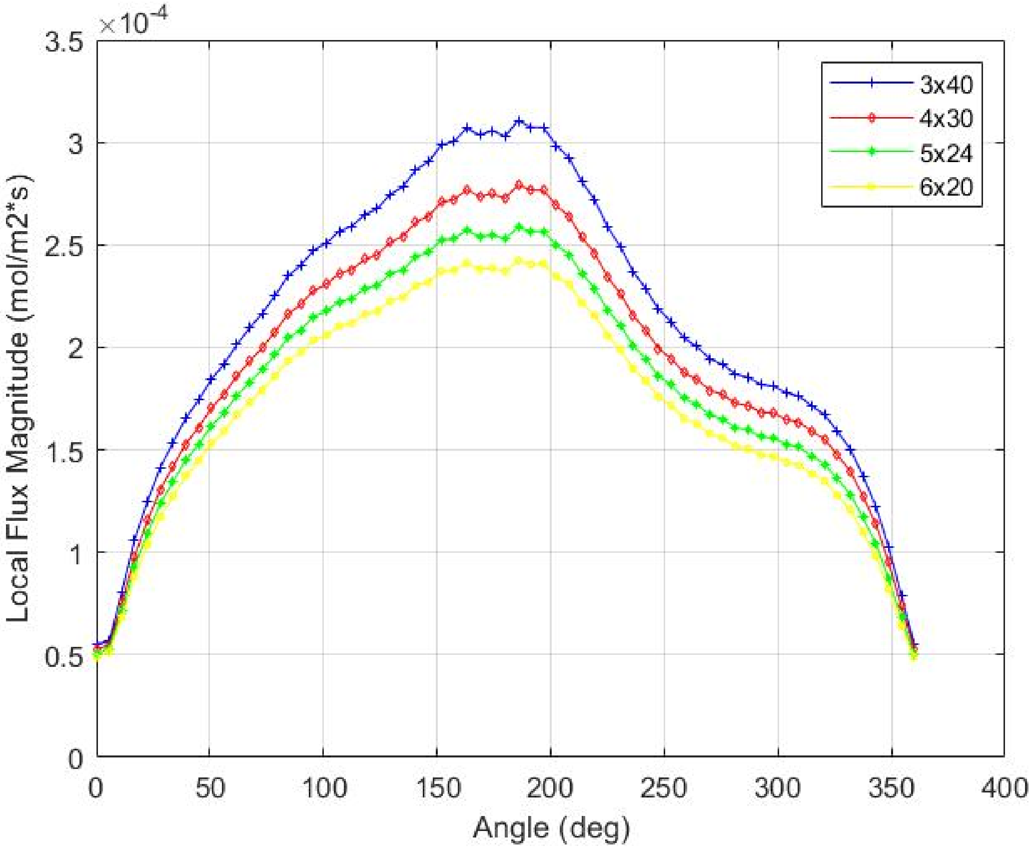

Figure 5.15. Local flux magnitude around the same membrane for all configurations.

Since peak oxygen transfer performance achieved in the Newtonian model at the leading edge cannot be achieved in the Carreau model, it is observed that the Carreau model is lower in time-averaged performance.

5.2.4. Shear Stress

The maximum WSS results, which are expected to have the greatest difference with Newtonian modeling, are given in Figure 5.16.

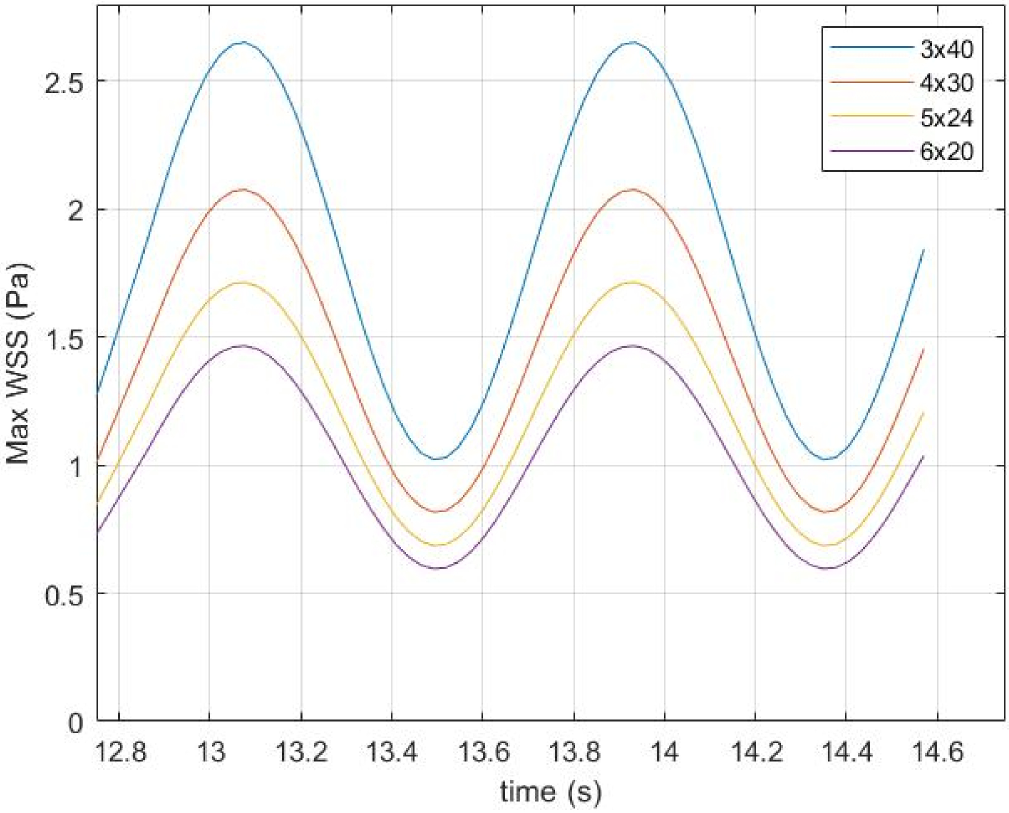

Figure 5.16. Maximum WSS values vs. time for different configurations.

As expected, the maximum WSS values obtained from the Carreau model are much higher than the values obtained from the Newtonian model. Although the Carreau model follows the same trend as the Newtonian model in terms of the increase in shear stress with increasing aspect ratio, the difference in magnitude leads to significant changes. As given in Section 5.2.1, the viscosity-shear rate relationship applied by the Carreau model shows shear stresses higher than the Newtonian model at shear rates lower than 100 s^{-1}. From this point of view, some configurations that meet the biocompatibility conditions in the Newtonian model exceed the maximum WSS limits in the Carreau model. In Table 5.9, time-averaged maximum WSS values are given for both Newtonian and Carreau models along with their percentile differences.

Table 5.9. Max WSS values comparison for Newtonian and Carreau models.

	$\mathbf{3 \times 40}$	$\mathbf{4 \times 30}$	$\mathbf{5 \times 24}$	$\mathbf{6 \times 20}$
Max WSS - Newtonian Model (Pa)	1.9481	1.4819	1.1931	0.9979
Max WSS - Carreau Model (Pa)	2.6670	2.0761	1.7191	1.4643
Percentile Difference (%)	36.90	40.10	44.09	46.74

It is noteworthy that as the aspect ratio decreases, the percentile difference for max WSS values between models increase. This is due to the fact that as the aspect ratio decreases, the average shear rate through the channel decreases and thus the shear stress increases to a greater extent.

It is seen that AR=24/5 and AR=20/6 configurations do not meet the biocompatibility conditions contrary to the results obtained in the Newtonian model. Therefore, AR=10/12 remains the only configuration likely to satisfy the biocompatibility requirements. The highest value AR=10/12 case has for maximum WSS is 0.8244 Pa, the lowest is 0.3566, and the time-averaged maximum WSS value of the configuration is 0.5942 Pa. Evaluating these results, the AR=10/12 is the only configuration meeting the biocompatibility requirements.

5.2.5. Non-Newtonian Results Evaluation and Discussion

When the results of four different geometries are examined, it is seen that only the AR=10/12 configuration is within the biocompatible limits, whereas the AR=20/6 configuration is deemed inadequate in fulfilling the current biocompatibility requirements.

The selected configurations for the Non-Newtonian model exhibit a narrower range of aspect ratios, resulting in closely aligned gas transfer outcomes. To assess whether the gas transfer performance converges similar to the Newtonian model, the saturation graph as a function of aspect ratio is presented in Figure 5.17.

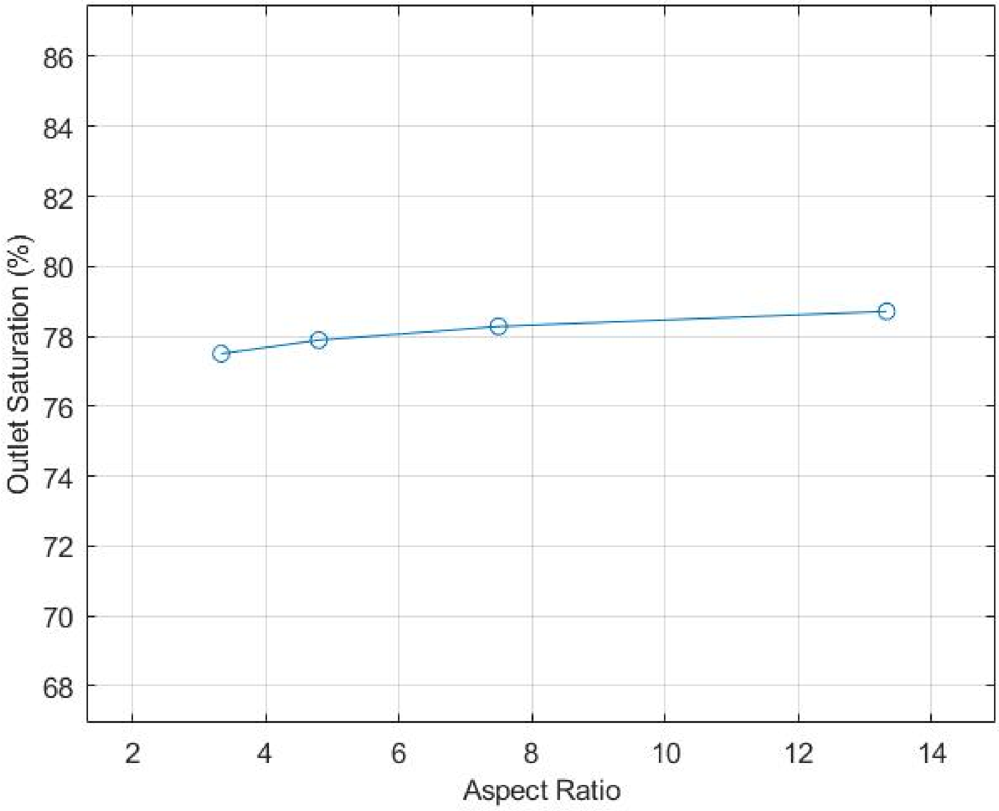

Figure 5.17. Time-averaged outlet saturation vs. aspect ratio for the Carreau model.

As depicted in Figure 5.17, it can be observed that the gas transfer performance converges.

The reasons for gas transfer to converge can be revealed similar to the Newtonian model by investigating the saturation throughout the channel and the oxygen transfer rate for each membrane column. In Figure 5.18, the average saturations of the section lines drawn from the middle of the membrane columns are shown and the same trend as in the Newtonian model is observed.

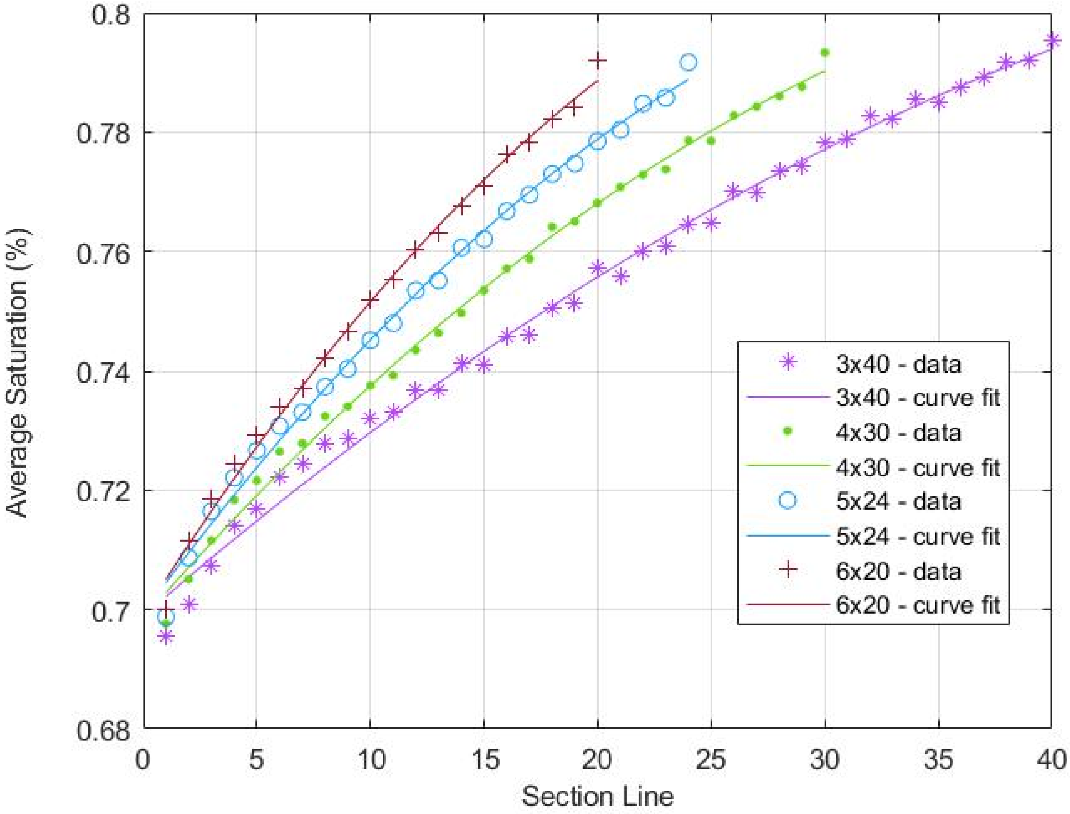

Figure 5.18. Average saturation in the section lines between columns for Carreau model.

While the increase in speed observed at higher aspect ratios is another factor to consider, the number of rows also play a vital role to determine the efficiency of a single fiber. The speed increase is directly linked to a constant volumetric flow rate and such a flow rate positively affects gas transfer performance for high aspect ratio configurations, in other words the configurations with small number of rows.

However, the presence of a larger number of rows plays a significant role in enhancing overall efficiency. This is particularly true for the efficiency observed in the first few columns. To provide a clearer understanding, Figure 5.19 offers a detailed breakdown. In this figure, the total gas transfer capabilities of the columns are shown. Each configuration is analyzed and presented separately, allowing for an in-depth comparison of their respective performances.

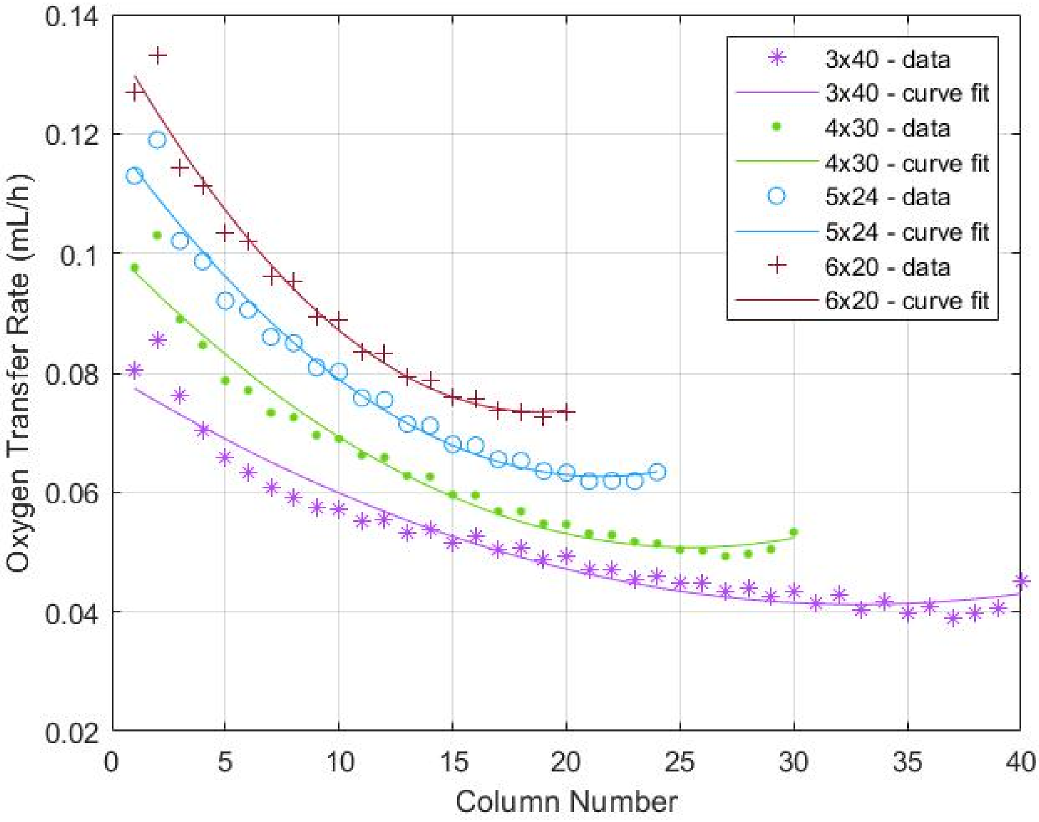

Figure 5.19. Total oxygen transfer rate of columns for Carreau model.

As a result of these, it has been suggested that geometries with AR=30/4 and AR=24/5 could be tested to obtain a configuration that is both biocompatible and has high gas transfer performance. The time-averaged outlet saturation vs. aspect ratio is given with added configurations in Figure 5.10 for comparison and showing the convergence.

As expected, new configurations perform better gas transfer rates than biocompatible configurations, namely AR=20/6 and AR=10/12. The fact that the AR=24/5 and AR=30/4 perform well compared to the AR=20/6 and AR=40/3 in terms of oxygen transfer performance is promising for these configurations. They have the potential to be an intermediate option that is both similar in oxygen transfer performance to the AR=40/3 configuration, which is just outside the biocompatible limits, and also is within acceptable biocompatible limits like the AR=20/6 configuration.

The maximum WSS values are investigated to evaluate the biocompatibility. The maximum WSS values oscillates between 0.6425 Pa and 1.9481 Pa with 1.2930 Pa on average for AR=40/3, between 0.4900 Pa and 1.4819 Pa with 0.9849 Pa on average for AR=30/4, between 0.3949 Pa and 1.1931 Pa with 0.7935 Pa on average for AR=24/5, and between 0.3304 Pa and 0.9979 Pa with 0.6639 Pa on average for AR=20/6. According to the maximum WSS values obtained, AR=24/5 configuration remains within the limits of biocompatibility, while AR=30/4 configuration is outside the acceptable limits during the peak flow rate. This makes the AR=24/5 configuration the most optimal choice. The fact that the oxygen transfer performance converges to a plateau with the increase of the aspect ratio value and that the AR=24/5 configuration is at the exact boundary in terms of WSS limits confirms this.

Pressure drops through the channel are given for the best alternatives in Newtonian Model in Table 5.10.

Table 5.10. Pressure drops for the best alternatives.

	3 × 40	**4 × 30**	**5 × 24**	**6 × 20**
Pressure Drop (Pa)	100.62	58.02	38.47	26.38

6. CONCLUSION

The flow analysis, gas transfer properties, pressure drops, and shear stress distributions of an average-sized cardiac-driven microfluidic artificial lung are investigated in various fiber bundle column to row aspect ratios with the same number of fibers. Under incompressible flow assumption, a numerical finite element study of blood flow and gas transport is performed for both Newtonian and Non-Newtonian Carreau models. It is sought to determine, taking into account all of the many aspects, the most suitable and efficient arrangement within physiological constraints.

There is no recirculation zone in any configuration at the current flow rates and pulsation amplitude. As a result, it is not observed blood being trapped in the wake region and negatively affecting the gas transfer. While the gas transfer improves and converges at some point as the aspect ratio increases, pressure drop and biocompatibility measures in terms of wall shear stress levels deteriorate incessantly, according to the study's findings. Another result is that for high aspect ratios, pulsatile conditions result in better overall gas transfer characteristics when compared to steady flow conditions. Additionally, pulsatile flow analysis proper to cardiac-driven devices is able to capture the shear stress fluctuations outside the biocompatible limits.

When Newtonian model outputs are evaluated, the AR=60/2, AR=30/4, AR=40/3, and AR=24/5 designs significantly outperform the AR=20/6 and AR=10/12 configurations in terms of gas transfer efficiency. The AR=30/4 configuration has a considerable pressure drop advantage over the AR=40/3 design. These two combinations, however, fall outside of the authorized maximum WSS values for EC coated membranes. The configurations with AR=24/5, AR=20/6, and AR=10/12 are designs that satisfy the requirements when the bio-compatibility restrictions are taken into account, with the AR=24/5 configuration having a crucial performance advantage over other two.

When the results of the non-Newtonian model are examined, similar trends are observed between the configurations except for the gas transfer. While gas transfer does not converge unlike the Newtonian model with increasing aspect ratio for the analyzed cases, pressure drop and shear stress values increase as in Newtonian model. The most important difference in this model is the variation of viscosity assumed in the Newtonian model. Shear rate is found to be less than 100 s^{-1} throughout the channel. Accordingly, changes in viscosity caused by shear rates in the Carreau model lead to serious differences in shear stress and pressure drop values compared to the Newtonian model. It is determined that AR=24/5 and AR=20/6 configurations, which are within the biocompatible limits in the Newtonian model, are out of the limits in the Carreu model. Among the analyzed geometries, the only configuration with a biocompatible design is AR=10/12.

In conclusion, there are many parameters that must be taken into account for the design efficiency of a cardiac-driven microfluidic artificial lung. In addition to these parameters, the solution method also has a significant effect on the results. The fact that the Carreau model shows great differences in shear stress results compared to the Newtonian model revealed the necessity of non-Newtonian modeling for a biocompatible design. Although there are minor differences in gas transfer between the two models, pressure drop and shear stress values should be obtained by non-Newtonian modeling for a holistic design. Likewise, the fact that the pulsatile modeling shows extreme values at peak flow moments and reveals significant differences compared to the steady-state model shows that the problem can only be solved correctly with pulsatile modeling.

REFERENCES

1. Quaderi, S. and J. Hurst, “The Unmet Global Burden of COPD”, *Global Health, Epidemiology and Genomics*, Vol. 3, pp. 82–84, 2018.

2. Lozano, R., M. Naghavi, K. Foreman, S. Lim, K. Shibuya, V. Aboyans, J. Abraham, T. Adair, R. Aggarwal and S. Y. Ahn, “Global and Regional Mortality from 235 Causes of Death for 20 Age Groups in 1990 and 2010: A Systematic Analysis for the Global Burden of Disease Study 2010”, *The Lancet*, Vol. 380, No. 9859, pp. 2095–2128, 2012.

3. Arens, J., O. Grottke, A. Haverich, L. S. Maier, T. Schmitz-Rode, U. Steinseifer, H. Wendel and R. Rossaint, “Toward a Long-term Artificial Lung”, *ASAIO Journal*, Vol. 66, No. 8, p. 847, 2020.

4. Kung, M., J. Lee, H. Kung and L. Mockros, “Microchannel Technologies for Artificial Lungs:(2) Screen-filled Wide Rectangular Channels”, *ASAIO Journal*, Vol. 54, No. 4, p. 383, 2008.

5. Thompson, A., L. Marks, M. Goudie, A. Rojas-Pena, H. Handa and J. Potkay, “A Small-scale, Rolled-membrane Microfluidic Artificial Lung Designed towards Future Large Area Manufacturing”, *Biomicrofluidics*, Vol. 11, No. 2, pp. 024–113, 2017.

6. Thi, B. P. N., B. T. D. Nguyen, I.-S. Jeong and J. F. Kim, “Hemocompatibility Challenge of Membrane Oxygenator for Artificial Lung Technology”, *Acta Biomaterialia*, Vol. 152, pp. 19–46, 2022.

7. Chan, K. Y., H. Fujioka, R. H. Bartlett, R. B. Hirschl and J. B. Grotberg, “Pulsatile Flow and Mass Transport over an Array of Cylinders: Gas Transfer in a Cardiac-Driven Artificial Lung”, *Journal of Biomechanical Engineering*, Vol. 128, No. 1,

pp. 85–96, 2006.

8. Taskin, M. E., K. H. Fraser, T. Zhang, B. P. Griffith and Z. J. Wu, "Micro-scale Modeling of Flow and Oxygen Transfer in Hollow-fiber Membrane Bundle", *Journal of Membrane Science*, Vol. 362, No. 1-2, pp. 172–183, 2010.

9. Gage, K. L., M. J. Gartner, G. W. Burgreen and W. R. Wagner, "Predicting Membrane Oxygenator Pressure Drop using Computational Fluid Dynamics", *Artificial Organs*, Vol. 26, No. 7, pp. 600–607, 2002.

10. Dierickx, P., D. De Wachter and P. Verdonck, "Blood Flow around Hollow Fibers", *The International Journal of Artificial Organs*, Vol. 23, No. 9, pp. 610–617, 2000.

11. Hormes, M., R. Borchardt, I. Mager, T. Schmitz-Rode, M. Behr and U. Steinseifer, "A Validated CFD Model to Predict O2 and CO2 Transfer within Hollow Fiber Membrane Oxygenators", *The International Journal of Artificial Organs*, Vol. 34, No. 3, pp. 317–325, 2011.

12. Kaesler, A., M. Rosen, T. Schmitz-Rode, U. Steinseifer and J. Arens, "Computational Modeling of Oxygen Transfer in Artificial Lungs", *Artificial Organs*, Vol. 42, No. 8, pp. 786–799, 2018.

13. Qiu, Y. and J. M. Tarbell, "Numerical Simulation of Pulsatile Flow in a Compliant Curved Tube Model of a Coronary Artery", *Journal of Biomechanical Engineering*, Vol. 122, No. 1, pp. 77–85, 2000.

14. Goldstick, T. K., V. T. Ciuryla and L. Zuckerman, "Diffusion of Oxygen in Plasma and Blood", *Oxygen Transport to Tissue—II*, pp. 183–190, Springer, 1976.

15. Berger, S. and L.-D. Jou, "Flows in Stenotic Vessels", *Annual Review of Fluid Mechanics*, Vol. 32, No. 1, pp. 347–382, 2000.

16. Cho, Y. I. and K. R. Kensey, "Effects of the Non-Newtonian Viscosity of Blood on

Flows in a Diseased Arterial Vessel. Part 1: Steady Flows", *Biorheology*, Vol. 28, No. 3-4, pp. 241–262, 1991.

17. Dierickx, P., D. De Wachter and P. Verdonck, "Two-dimensional Finite Element Model for Oxygen Transfer in Cross-flow Hollow Fiber Membrane Artificial Lungs", *The International Journal of Artificial Organs*, Vol. 24, No. 9, pp. 628–635, 2001.

18. Kannel, W. B., C. Kannel, R. S. Paffenbarger Jr and L. A. Cupples, "Heart Rate and Cardiovascular Mortality: the Framingham Study", *American Heart Journal*, Vol. 113, No. 6, pp. 1489–1494, 1987.

19. Collins, J.-A., A. Rudenski, J. Gibson, L. Howard and R. O'Driscoll, "Relating Oxygen Partial Pressure, Saturation and Content: The Haemoglobin-Oxygen Dissociation Curve", *Breathe*, Vol. 11, No. 3, pp. 194–201, 2015.

20. Zierenberg, J. R., H. Fujioka, K. E. Cook and J. B. Grotberg, "Pulsatile Flow and Oxygen Transport past Cylindrical Fiber Arrays for an Artificial Lung: Computational and Experimental Studies", *Journal of Biomechanical Engineering*, Vol. 130, pp. 1–12, 2008.

21. Vaslef, S. N., L. F. Mockros, R. W. Anderson and R. J. Leonard, "Use of a Mathematical Model to Predict Oxygen Transfer Rates in Hollow Fiber Membrane Oxygenators.", *ASAIO journal*, Vol. 40, No. 4, pp. 990–996, 1994.

22. Keller, J. B., "Viscous Flow through a Grating or Lattice of Cylinders", *Journal of Fluid Mechanics*, Vol. 18, No. 1, pp. 94–96, 1964.

23. Incropera, F. P., D. P. DeWitt, T. L. Bergman and A. S. Lavine, *Fundamentals of Heat and Mass Transfer*, Vol. 6, Wiley New York, 1996.

24. Churchill, S. and M. Bernstein, "A Correlating Equation for Forced Convection from Gases and Liquids to a Circular Cylinder in Crossflow", *Journal of Heat Transfer*, Vol. 99, No. 2, pp. 300–306, 1977.

25. Low, K. W., R. Van Loon, S. A. Rolland and J. Sienz, “Formulation of Generalized Mass Transfer Correlations for Blood Oxygenator Design”, *Journal of Biomechanical Engineering*, Vol. 139, No. 3, pp. 031–007, 2017.

26. Hellmann, A., S. Klein, F. Hesselmann, S. Djeljadini, T. Schmitz-Rode, S. Jockenhoevel, C. G. Cornelissen and A. L. Thiebes, “EndOxy: Mid-term Stability and Shear Stress Resistance of Endothelial Cells on PDMS Gas Exchange Membranes”, *Artificial Organs*, Vol. 44, No. 10, pp. E419–E433, 2020.

27. Hathcock, J. J., “Flow Effects on Coagulation and Thrombosis”, *Arteriosclerosis, Thrombosis, and Vascular Biology*, Vol. 26, No. 8, pp. 1729–1737, 2006.

28. Falati, S., Q. Liu, P. Gross, G. Merrill-Skoloff, J. Chou, E. Vandendries, A. Celi, K. Croce, B. C. Furie and B. Furie, “Accumulation of Tissue Factor into Developing Thrombi in Vivo is Dependent upon Microparticle P-selectin Glycoprotein Ligand 1 and Platelet P-selectin”, *The Journal of Experimental Medicine*, Vol. 197, No. 11, pp. 1585–1598, 2003.

29. Bilgi, C. and K. Atalık, “Effects of Blood Viscoelasticity on Pulsatile Hemodynamics in Arterial Aneurysms”, *Journal of Non-Newtonian Fluid Mechanics*, Vol. 279, p. 104263, 2020.